Visualization of CH_4/CO_2 hydrate dissociation and reformation during multistep depressurization assisted by pore-scale X-ray computed tomography

Ouyang, Qian; Pandey, Jyoti Shanker; Xu, Yao; Solms, Nicolas von

Published in:
Gas Science and Engineering

Link to article, DOI:
10.1016/j.jgsce.2023.204952

Publication date:
2023

Document Version
Publisher's PDF, also known as Version of record

113 (2023) 204952

Contents lists available at ScienceDirect

Gas Science and Engineering

journal homepage: www.journals.elsevier.com/gas-science-and-engineering

Visualization of CH_4/CO_2 hydrate dissociation and reformation during multistep depressurization assisted by pore-scale X-ray computed tomography

Qian Ouyang, Jyoti Shanker Pandey *, Yao Xu, Nicolas von Solms **

Center for Energy Resource Engineering (CERE), Department of Chemical Engineering, Technical University of Denmark, 2800 Kgs. Lyngby, Denmark

ARTICLE INFO

Keywords:
Natural gas hydrates
Multistep depressurization
Hydrate morphologies
Fluid migration
X-ray CT

ABSTRACT

CH_4–CO_2 swapping is a promising and safe technique to produce CH_4 gas and store CO_2 without destabilizing hydrate-bearing sediments. However, inefficient CH_4 recovery due to low CO_2 diffusion prevents this technique from large-scale application. Multistep depressurization (MD) is therefore performed on CH_4/CO_2 hydrates after hydrate swapping to improve CO_2 diffusion. This work presents pore-scale visualization of CH_4/CO_2 hydrates during MD by non-destructive X-ray computed tomography (CT) and combines the visual results with mixed hydrate kinetics to study hydrate morphology evolution and fluid migration. Influences of particle sizes (2–5 mm) and L-methionine (3000 ppm) on dissociation parameters were examined at reducing depletion pressures (8.5–59.4 bar) and constant temperatures (0.5–1.3 °C). The results of CT images showed enlargements of hydrate or gas phase with depletion pressures below CH_4 hydrate stability pressures, complying with the pressure variations during MD. These variations of hydrate and fluid phases as well as pressure responses were the most obvious for particle size of 3 mm, resulted from good pore connectivity and relatively efficient mass transfer. L-methionine had no direct effect on CH_4 production but enhanced CO_2 storage, with the highest both CH_4 gaseous mole fraction (86.1 mol%) and CO_2 storage ratio (88.8%) at depletion pressure of 22.6 bar. This work clarified five-type pressure variations coupled with phase changes, providing firm evidence for hydrate dissociation/reformation and fluid migration that greatly affected hydrate exploitation. These understandings of varying morphologies and compositions of CH_4/CO_2 hydrates during MD would be applicable to help hydrate energy harvest and carbon emission mitigation.

1. Introduction

Natural gas hydrates (NGHs) are non-stoichiometric clathrate crystal substances formed by water and hydrocarbon gases such as CH_4 and C_2H_6 (Sloan and Koh, 2007). Formation and stability of NGHs need relatively high pressure and low temperature. These thermodynamic conditions exist in oceanic sediments where hydrate occurrence is usually a type of pore-filling, and in permafrost areas where hydrate occurrence is usually a type of cementing (Max, 2003; Zhao et al., 2021). The estimated reserve of natural gas stored in global NGHs is 3×10^{15} m^3 (Boswell and Collett, 2011), compared with 4.32×10^{14} m^3 in conventional gas resources and $(1.93–4.54) \times 10^{14}$ m^3 in shale gas reservoirs (McGlade et al., 2013). Such a huge amount of reserve makes NGHs a potential dominant energy resource.

Greenhouse gas emissions (CO_2 as a major contributor) are predicted to increase by 28% by 2030 (Qureshi et al., 2021), which poses a severe threat on environment and climate. European Union has proposed a reduction target of CO_2 emissions by 80% by 2050 (Abu Hassan et al., 2020). CO_2 capture and storage (CCS) is a prospective and emerging technique to achieve this reduction target (L'Orange Seigo et al., 2014; Zeman, 2007), and many efforts are being made to enhance its economy (Abu Hassan et al., 2020; Pandey et al., 2022a). Specifically, the estimated cost of CO_2 elimination is 20–40 $/ton CO_2 by hydrate-based capture and that of CO_2 storage in ocean is 5–30 $/ton CO_2 (Nguyen et al., 2022). Success of CO_2 elimination relies on CO_2 capture efficiency, while benefit of CO_2 storage depends on CO_2 hydrate formation potential. To harness huge storage capacity of ocean, addition of environmental-friendly promotors, e.g. amino acids could be

* Corresponding author.
** Corresponding author.
E-mail addresses: jyshp@kt.dtu.dk (J.S. Pandey), nvs@kt.dtu.dk (N. von Solms).

https://doi.org/10.1016/j.jgsce.2023.204952
Received 15 October 2022; Received in revised form 24 February 2023; Accepted 13 March 2023
Available online 15 March 2023

prospective to facilitate CO_2 hydrate formation kinetics (Bavoh et al., 2019).

Alternatively, expenditure of CO_2 hydrate storage can be compensated by simultaneous CH_4 gas recovery through CH_4–CO_2 swapping exploitation. This CH_4–CO_2 swapping is realized with one CO_2 molecule replacing one CH_4 molecule without water production and stratum failure (Cha et al., 2015). This carbon-neutral process makes swapping technique more competitive compared with other exploitation methods, such as depressurization (Shi et al., 2021), thermal stimulation (Tupsakhare et al., 2017) and chemical inhibitor injection (Li et al., 2017). However, swapping efficiencies including reaction rate and CH_4 recovery are low due to mass transfer barriers caused by CO_2 hydrate formation (Davies et al., 2010).

To mitigate this problem of low exploitation efficiency, one of the strategies is to combine swapping with depressurization. Depressurization is regarded as the most economical method to exploit hydrates due to its simple operation and low production cost (Chen et al., 2018). The idea of this combination method is that depressurization decomposes CH_4/CO_2 hydrates around unexploited CH_4 hydrates and thus creates diffusion channels for CO_2 penetration. Many researchers have proved the feasibility and efficiency of this combination method (Chen et al., 2019; Pandey and Solms, 2019; Zhao et al., 2016a). However, rapid/direct depressurization induces fast hydrate dissociation and a shortage of heat supply. This tends to cause ice generation and secondary hydrate formation. Slow depressurization is therefore employed to dissociate hydrates in well-controlled manners. As one of slow depressurization methods, multistep depressurization refers to depletions conducted in multiple stages with suitable pressure ranges (Heeschen et al., 2016; Phillips et al., 2019; Yang et al., 2019). This method can effectively alleviate Joule-Thomson effect which resulted from rapid gas flow and retarded speed of hydrate decomposition, and thus addressing problems of ice and secondary hydrate due to low temperature and insufficient heat (Li et al., 2020). A summary of exploitation methods with a focus of depressurization is presented in Fig. 1.

Multistep depressurization on CH_4/CO_2 hydrates to exploit CH_4 hydrates and store CO_2 hydrates is a complex process of phase transition and gas-water flow. The natures of hydrate-bearing sediments (HBS) such as fluid saturation, distribution and permeability are the dominant factor controlling exploitation efficiencies. X-ray computed tomography (CT) is an effective and non-destructive technique to visualize microstructures and characterize fluid phases within HBS (Mikami et al., 2006). Tomutsa et al. (2002) imaged a dissociation front in hydrate/-sand samples by CT to distinguish hydrate-bearing samples and hydrate-dissociating samples. Jin et al. (2004, 2006) employed micro-focus CT to characterize free-gas spaces, sand particles and hydrate or ice. Kneafsey et al. (2007) performed CT tests for thermal properties of samples and hydrate dissociation kinetics, finding water migration and mineral grain shifting. Zhao et al. (2016b) investigated hydrate structural with different particle sizes by micro-CT, verifying uniformly distributed hydrates almost filling pore spaces. 3D image visualization can characterize hydrate morphologies and fluid properties more clearly. Wu et al. (2020) developed a 3D morphological modeling algorithm and found growth patterns of cementing hydrate. Similarly, Wang et al. (2018) observed grain-cementing hydrates mainly grew and pore-filling hydrates existed only during intermediate stages by 3D images.

The studies above investigated physical properties of HBS, occurrence modes of hydrates and hydrate morphologies, as summarized in Fig. 2(a). Fluid behaviors and gas production during hydrate exploitation are dependent on porosity, saturation, and especially permeability. The occurrence modes of hydrates can be summarized into five types, i.e. pore-filling, cementing, grain-coating, load-bearing and patchy cluster (Dai et al., 2012; Lv et al., 2020), as exhibited in Fig. 2(b). These occurrence types of hydrates were mainly caused by driving force, sand and fluid properties, and gas-water distribution. However, above-mentioned studies reported independent morphological CH_4 hydrate formation or dissociation within HBS. Little attention has been paid to varying hydrate patterns and water-gas migration during multistep depressurization on CH_4/CO_2 mixed hydrates, which are crucial for efficient gas production and carbon storage.

Fig. 3 presents the main research focuses in previous works, recent works and this work. Previous studies showed that combination of hydrate swapping with multistep depressurization benefits increase of CO_2 sweep area and CH_4 gas production, decrease of water production and prevention of ice and hydrate formation (Chen et al., 2019; Pandey et al., 2021a; Zhao et al., 2016a). Our previous studies independently observed hydrate reformation and dissociation in microfluidic chips (Pandey et al., 2021c, 2022c). One recent study individually speculated variations of CH_4-rich hydrates and CO_2-rich hydrates by pressure variations and gas compositions (Pandey et al., 2022b). The other two recent studies confirmed the feasibility and efficiency of multistep depressurization on CH_4/CO_2 hydrates, and affirmed the critical parameters determining kinetics of this method (Ouyang et al., 2022a, 2022b). However, there is a still lack of visual evidence and further knowledge on whether CH_4/CO_2 hydrates can be slowly depressurized after CO_2 injection, and simultaneously how the mixed hydrate morphologies vary during depressurization. It is still unclear how fluid migration and hydrate distribution in HBS affect CH_4 gas recovery and CO_2 hydrate storage.

Thus, in this work, CH_4/CO_2 hydrates (CH_4-rich) were formed in artificial cores with different particle sizes and different solutions (water/L-methionine) to simulate the mixed hydrates after depressurization and hydrate swapping. Depletions were conducted periodically on CH_4/CO_2 hydrates to trigger multistep depressurization. Visual evidence of gas-water-hydrate variations during exploitation was acquired

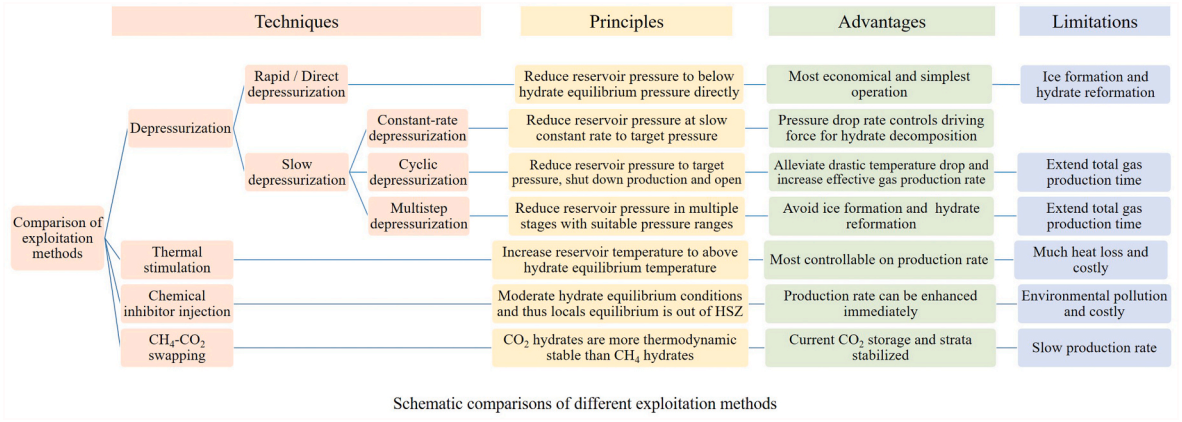

Fig. 1. Schematic of different exploitation methods with focus of depressurization.

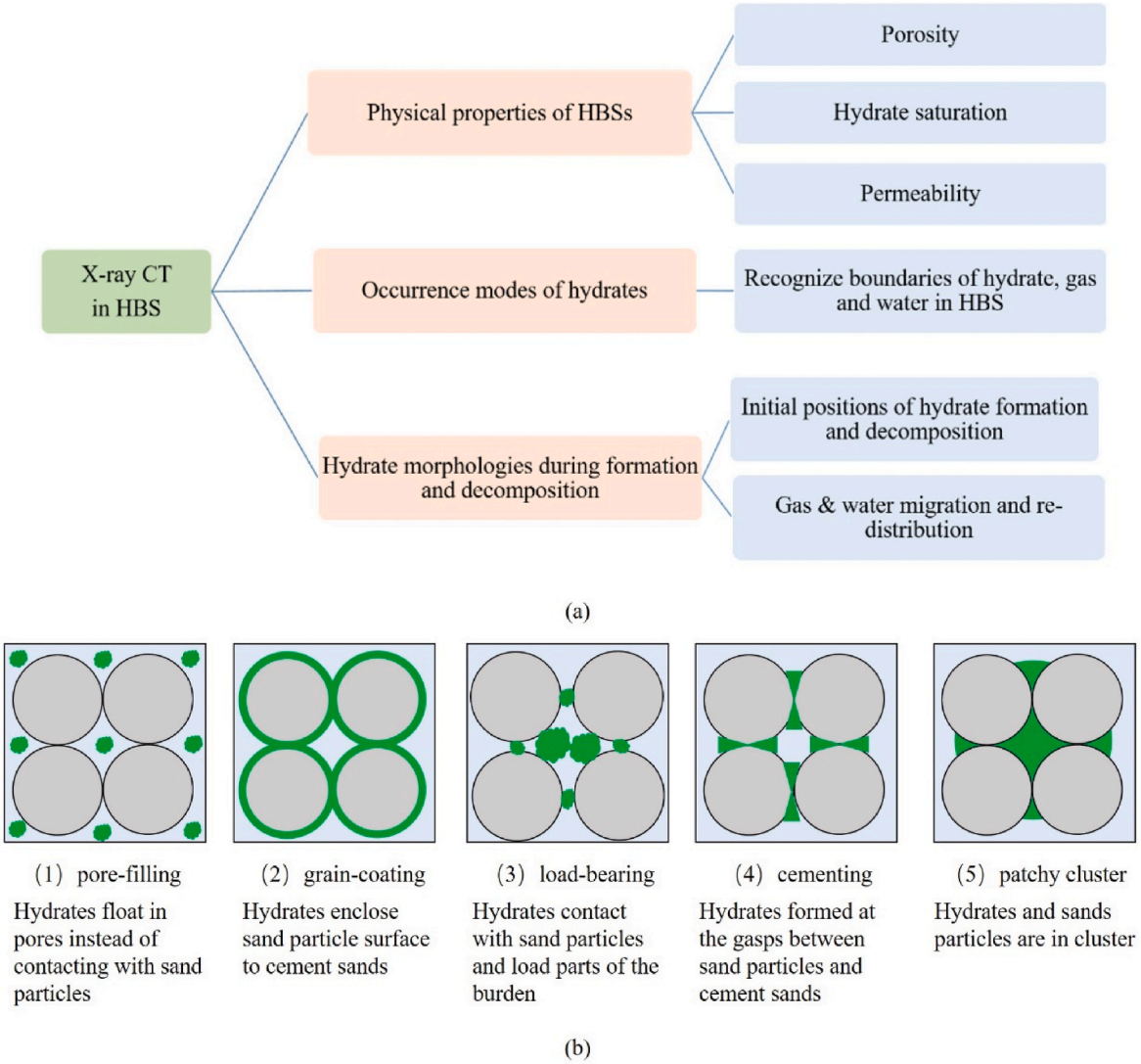

Fig. 2. Schematic of: (a) investigation scope of X-ray CT in HBS, and (b) types of HBS (Dai et al., 2012; Lv et al., 2020).

by CT technique. Hydrate morphological changes and CT values were coupled to verify the corresponding hydrate reformation/dissociation and to correlate with kinetic analysis of multistep depressurization. The purposes were to: (1) test whether CH_4/CO_2 mixed hydrates can be slowly depressurized after CO_2 injection; (2) observe how their morphologies vary during depressurization; and (3) explore effects of fluid migration and hydrate distribution on CH_4 gas recovery and CO_2 hydrate storage. The observations and findings can further expand research on this method and accelerate the transition from experimental to pilot-scale testing.

2. Methodology

2.1. Materials and setup

Glass beads (hydrophilic, VWR European Cat. No, Glasperlen KS) with diameters of 2 mm, 3 mm and 5 mm and density of 2.5 g/cm^3 were used to generate artificial core. The selection of this range of diameter was the result of trial and error in the in-house CT setup. Pore space was not visible in a smaller range (less than 2 mm) and gas hydrates were of bulk nature in a larger range (over 5 mm). This range of diameter also refers to those of 0.85–7.0 mm in many references on hydrate CT studies (Iassonov et al., 2009; Song et al., 2013; Ta et al., 2015; Wang et al., 2020; Zhao et al., 2016b). An artificial core sample consisting 5 mm (top) and 2 mm (down) glass beads was shown for visualization only in Fig. 4. A mixed gas of 70 mol%CH_4/CO_2 (Air Liquide Corporation, Denmark) was used to form CH_4/CO_2 mixed hydrates. Deionized water was produced (resistivity of 18.25 mΩ cm^{-1}) in laboratory. L-methionine (Sigma Aldrich Corporation) was prepared in a concentration of 3000 ppm.

An X-ray CT system was employed to observe distribution and dynamic change of hydrates in artificial core, as shown in Fig. 4. The X-ray CT system mainly includes a medical X-ray CT setup (Somatom Plus 4, Siemens CT product) and a core holder, as shown in Fig. 5. The core holder has a maximum operating pressure of 200 bar, with two caps sealed at two sides. P1 was inlet & outlet side, PM was middle side and P2 was blind side. The core holder was wrapped into a fluid jacket, with temperature controlled by a cooling bath (Julabo FPW50-HE). Two thermocouples ranging with a precision of 0.01 °C were placed at confining space and edge of core. A differential pressure transducer was installed at two sides of core. Confining pressure was supplied by a syringe pump (Teledyne, ISCO) through injection of deionized water and exerted on a rubber sleeve. A pressure gauge was used to show confining pressure. Temperatures and pressures were recorded in a data collector (Agilent 34972 A, Agilent Tech.) at each 10s. Gas samples were collected and transmitted to a micro gas chromatography (Agilent, micro-GC 490) for composition analysis.

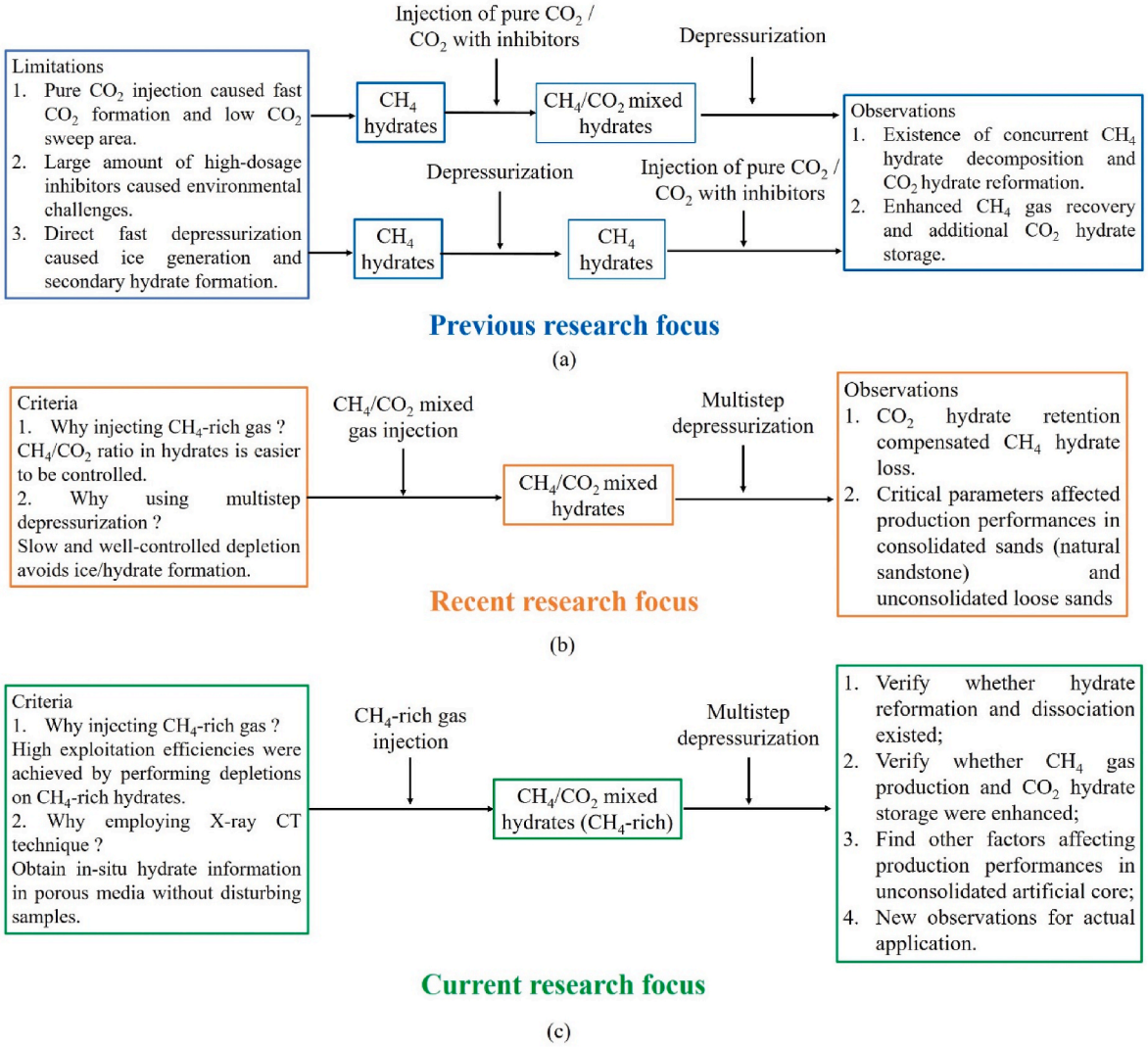

Fig. 3. Schematic diagram of research focus in: (a) previous works (Chen et al., 2019; Pandey et al., 2021c, 2022c; Zhao et al., 2016a); (b) recent works (Ouyang et al., 2022a, 2022b; Pandey et al., 2022b) and (c) current work. CH_4-rich means CH_4 to CO_2 ratio in mole amount over 1.

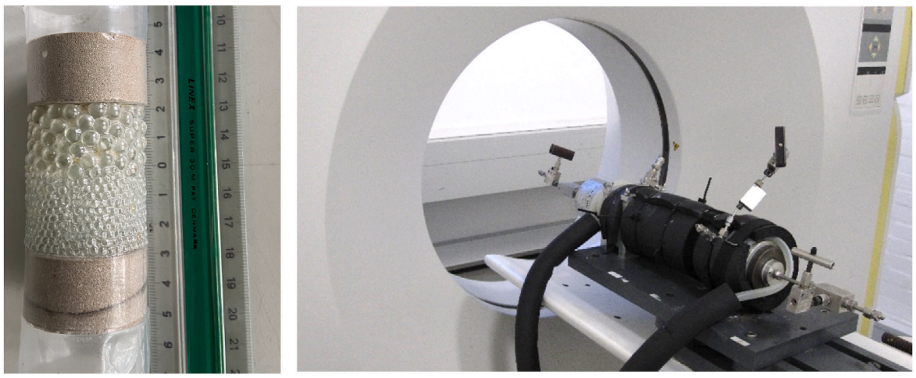

Fig. 4. Pictures of artificial core (left), CT setup and core holder (right).

2.2. Experimental procedures

2.2.1. Artificial core preparation

A certain weight of clean and dry glass beads was employed to fabricate artificial core. The length of artificial core was 3 cm or 5 cm with a diameter of 4 cm. Pore volume of dry core samples was calculated to determine the amount of deionized water for 50% initial water saturation. The core sample was wrapped tightly with a rubber sleeve and then placed inside core holder. Next, two caps were installed at two sides of core to implement inward pressing. Then, confining water injection was conducted through an ISCO pump to generate confining pressure of 110 bar around the core. After vacuuming for 10 min to

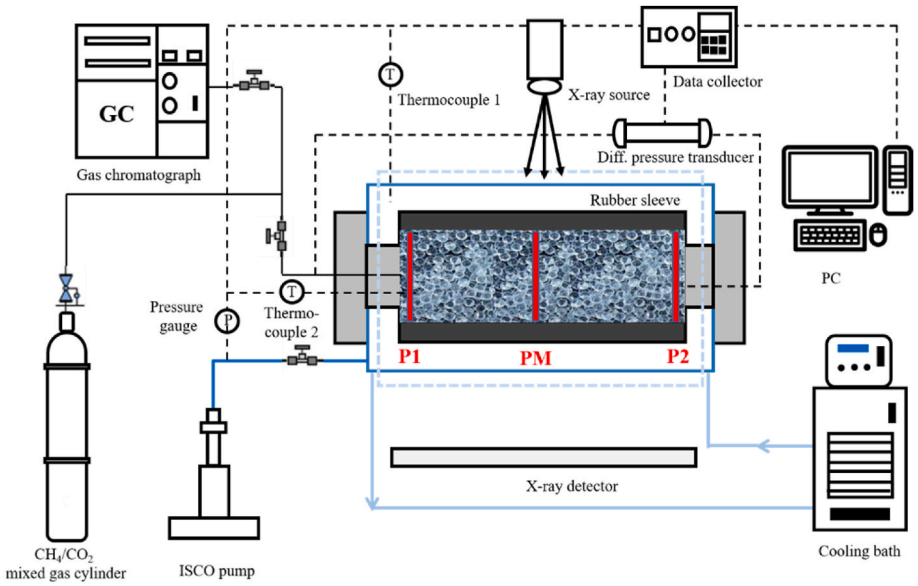

Fig. 5. Schematic of experimental setup for hydrate formation and multistep depressurization.

ensure absence of air, core was scanned with the CT setup to obtain images of dry porous media.

2.2.2. Hydrate formation

A determined amount of deionized water was injected into core through ISCO pump. Afterward, core holder was pressurized with CH_4/CO_2 mixed gas until core pressure increased to 80–85 bar. After core pressure stabilized for 2 h, the working temperature of cooling bath was set to the desired value to induce hydrate formation under constant volume conditions. Hereafter, core pressure dropped gradually due to hydrate formation. When core pressure stayed unchanged for 12 h, process of hydrate formation was considered completed. The strategy of three cycles of cooling & heating (annealing process) was employed to improve hydrate formation and water-gas distribution (Farahani et al., 2021; Yin et al., 2019). Table 1 provides the detailed experimental conditions for CH_4/CO_2 hydrate formation for Exp1-4.

2.2.3. Multistep depressurization

After annealing process for hydrate formation, multistep depressurization was repeated every 4 hours (shut-in period) by controlling the valve at P1 in Fig. 5 to reduce core pressure, i.e. stepped depletion. This was due to the trade-off between shut-in period and recovery/storage efficiency for actual implementation, i.e. short interval may shorten production period (almost like constant-rate depressurization) but reduce overall productivity, and a long interval may prolong production period but effectively enable CO_2 storage. The shut-in period was employed because it provided sufficient time for gas/water migration and mixture. This time window was for hydrate nucleation and growth during hydrate reformation in the stability zone between CH_4 and CO_2 hydrates. As nucleation is a stochastic phenomenon, 4-hour shut-in period was found to the optimized interval that could facilitate maximum efficiency (Ouyang et al., 2022a). Gas samples were collected and analyzed by in-line GC to obtain gas compositions. This process of stepped depletions proceeded until core pressure was reduced close to or under CO_2 hydrate stability pressure.

2.2.4. CT scanning

CT scanning work was performed: (1) one for dry core, (2) one for core after water and gas injection, (3) three for core after 1st/2nd/3rd cooling, and (4) multiple numbers for core sample just before and after multistep depressurization. The CT setup has an unsigned 16-bit pixel grayscale. All CT scanning operations were conducted at same parameters: a source voltage of 120 kV and an electric current of 170 mA, with the exposure time set at 2.0 s. The field of view (FOV) was fixed at center of core to focus on pores where hydrate formed and dissociated. The distance for each slice was 1 mm and a group of 30 images was collected for each core. The scanning covered a cross-sectional area of 82 mm × 82 mm and per scan was transformed into a two-dimensional (2D) 512 × 512 image array of picture elements. The image of DICOM format signed 16-bit grayscale has a resolution of 6.2 pixels/mm. The quality of these images was dependent on the resolution of CT setup. The 2D images shown in this work were cropped in software ImageJ. The cropped CT images were then processed to obtain CT values and histogram data.

2.2.5. CT image process

To observe phase distribution and migration within core, color difference segmentation based on CT value was conducted on CT images by mathematical software Matlab. This method was based on references (Jin et al., 2004, 2006; Sato et al., 2005). All CT images obeyed the same processing procedures, as shown in Fig. 6. Different gray values in original CT images represent different attenuation coefficients of X-ray, which are determined by density of substances (gas, water, hydrate and glass bead). Correspondingly, the grayscale from 0 (off as seen in black) to 255 (white as seen in brightest) can be transformed into a color map

Table 1
Summary of artificial core properties and CH_4/CO_2 hydrate formation parameters at Exp1-4.

No.	Bead diameter (mm)	Core dimensions (length × diameter, mm)	Porosity (%)	Weight of dry core (g)	Solution	Initial pressure (bar)	Final pressure (bar)	Temperature (°C)	Initial water saturation (%)
Exp1	2	30 × 40	41.20	55.0	Water	87.2	59.4	1.00	52.7
Exp2	3	30 × 40	41.72	47.0	Water	87.6	41.9	1.32	54.0
Exp3	5	50 × 40	32.55	80.5	Water	75.7	29.3	0.50	54.7
Exp4	3	30 × 40	38.86	49.3	L-meth	86.1	53.6	0.54	50.0

The concentration of L-methionine (L-meth) is 3000 ppm.

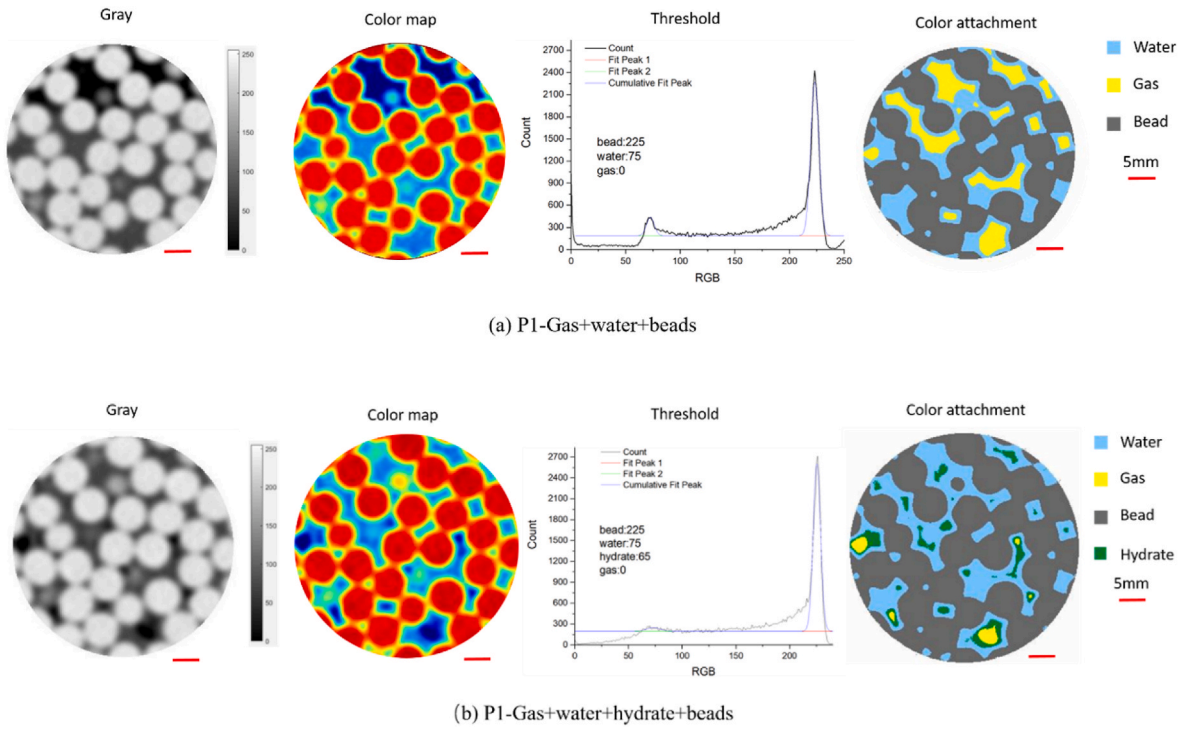

Fig. 6. Color attachment on CT images by threshold method: (a) three phases of gas, water, and beads before hydrate formation; (b) four phases of gas, water, hydrate and beads after hydrate formation. The segment CT images are processed by ImageJ and Matlab.

of RGB (Red, Green and Blue) range (0–255) for distinguishment. However, it was still difficult to distinguish water and hydrates which have similar densities (0.9 g/cm^3 for hydrates and 1.0 g/cm^3 for water). Thus, threshold method was adapted for phase characterization based on references (He et al., 2018; Lei et al., 2018; Sadeq et al., 2018), as confirmed in Fig. 6(a) that RGB ranges in sample before hydrate formation: (0–60) for gas, (60–90) for water, and (90–255) for beads; Fig. 6 (b) that RGB ranges in sample after hydrate formation: (0–60) for gas, (60–70) for hydrate, (70–90) for water and (90–255) for beads. Thus, grayscale CT images can be attached with segmented colors to characterize different phases in all scenarios.

2.2.6. Calculation

The calculations for hydrate formation and multistep depressurization are described in Appendix A.

3. Results and discussions

3.1. Characteristics of CH_4/CO_2 hydrates during formation

Characteristics of CH_4/CO_2 hydrate formation included pressure-temperature, normalized CT values (NCT) and gas-water-hydrate phase changes. These kinetic data and characterized images can provide comprehensive information on phase transitions and fluid distribution during hydrate formation.

3.1.1. Hydrate formation patterns in water

Fig. 7(a) presents variations of pressure-temperature and normalized CT value together with the processed CT images. For CH_4/CO_2 hydrate formation with pure water at Exp1, initial pressure drops caused by gas consumption were detected during 1st cooling process. Similar pressure drops during 2nd & 3rd cooling process appeared earlier than that during 1st cooling process, indicating induction time for hydrate formation was significantly shortened with annealing process. This phenomenon is consistent with the memory effect reported in (Kou et al., 2022; Uchida et al., 2016). Hydrate formation was confirmed by a pressure differential between P1 and P2, which was attributed to hydrate blockage within pores in core sample. Additionally, a sudden pressure drop was shown during 1st cooling in Fig. 7(a) and it was attributed to pressure compromise between high-pressure zone at P1 and low-pressure zone elsewhere.

The initial values of CT were normalized to 1.00 (NCT) for three positions of core, i.e. P1 at inlet & outlet side, PM at middle side and P2 at blind side, as shown in Fig. 5. It was found that these three values decreased to same amount (below 1.00) at the end of 1st cooling. This was cused by homogeneous hydrate formation within core among three positions because CT value of hydrate was lower than that of water. Afterward, all three NCT values increased back to 1.00 after 1st heating, indicating all hydrates dissociated at three positions. Comparatively, NCT (P2) increased to 1.06 while the other two to almost 1.00 just before 2nd cooling, denoting more water phase occupying the cross-section than that just before 1st cooling. This supported gas-water redistribution through annealing process. The final values of NCT were 0.98–1.00 for three positions, which affirmed a good homogeneity of gas-water-hydrate distribution along the core.

P1 cross-section was selected for further analysis of gas-water-hydrate distribution given it was close to the gas injection point for hydrate formation and gas release point for stepped depletion. Fig. 7(b) provides information on phases of gas, water and hydrate in terms of P1 cross-section. Gas and water were distributed dispersedly initially (t = 0 h) because of capillary force in pores and hydrophilicity of glass beads. Afterward, hydrates formed around gas phase after 1st cooling (t = 14.5 h). This complied with NCT (P1) values below 1.00, indicating hydrate formation above-mentioned. However, NCT (P1) increased to over 1.00 after 2nd cooling (t = 28.5 h). This may be attributed to water migration which can be detected as water phase shrinkage in the hollow white rectangle of Fig. 7(b). The water migration resulted from capillary pressure. Meanwhile, solid bead phase enlargement was observed in Fig. 7(b). Hydrate formation and dissociation caused different pressure zones during annealing process. This forced particles to move slightly between pressure zones, or between pressure zones and high confining pressure (110 bar). Slight movement of particles would therefore

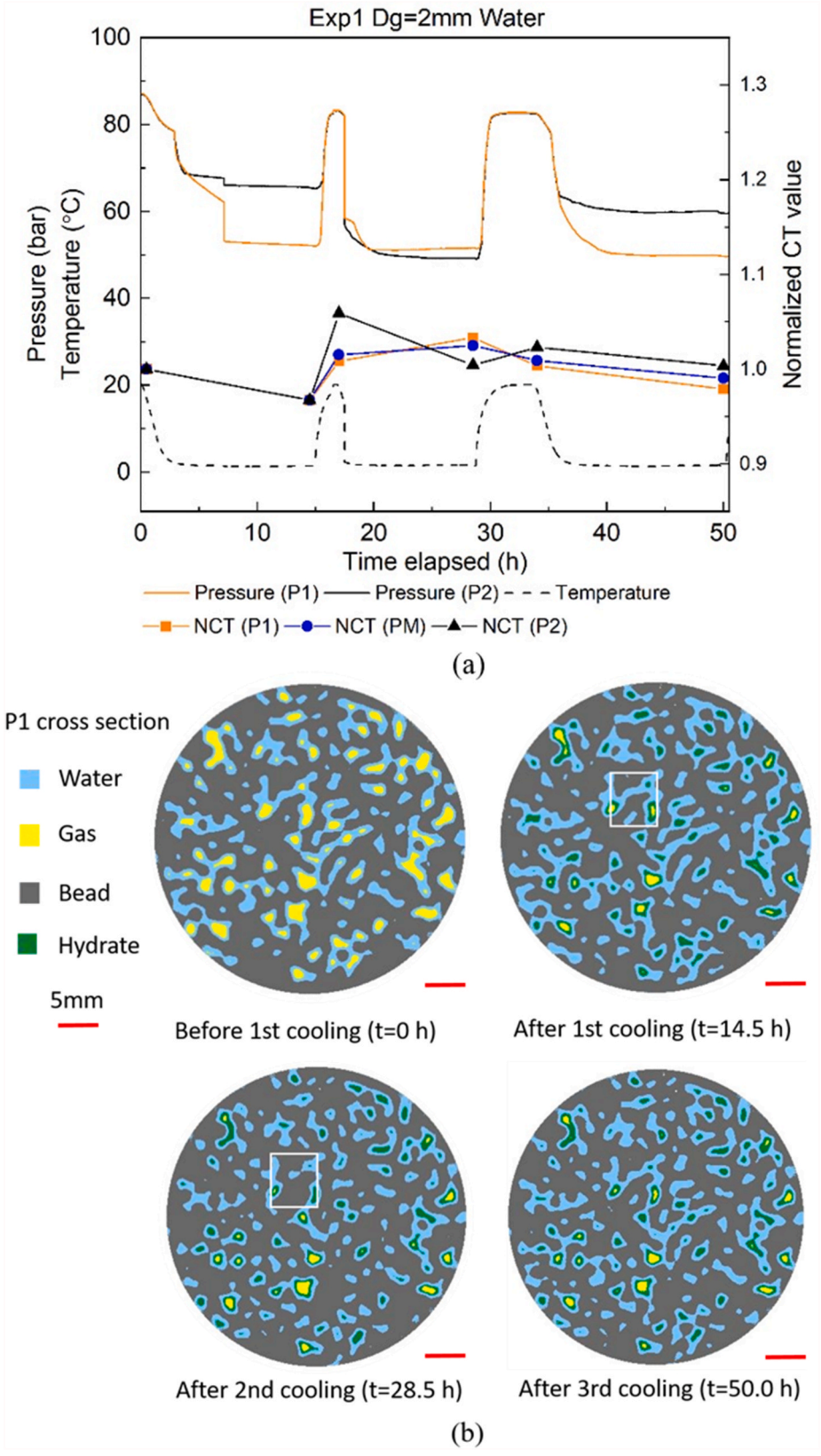

Fig. 7. Characteristics of CH_4/CO_2 hydrate formation during multiple cooling & heating for pure water at Exp1 (D_g = 2 mm): (a) variations of pressures, temperatures and normalized CT (NCT) values and, (b) 2D images at P1 cross-section for phase characterization. The hollow white rectangle is for comparison at the same position.

increase/decrease the solid bead phase at cross-section as shown in CT images. These water phase shrinkage and solid bead phase enlargement therefore increased local CT values. Nevertheless, water appeared in the same area after 3rd cooling (t = 50.0 h), causing decrease of NCT (P1) and redistribution of gas-water-hydrate after annealing process.

The types and occurrences of hydrates in core were analyzed in Fig. 7 (b). It was identified that dispersed pore-filling rather than grain-coating or cementing hydrates formed in pore spaces. Generally, hydrate nuclei and crystals generated firstly at gas-water interfaces. And the hydrates were found to nucleate heterogeneously in porous media with gas and sediments, consistent with the findings in references (Englezos et al., 1987; Song et al., 2013). In some pore spaces, the hydrate clusters formed around continuous gas phase until they consumed all gases. In other pore spaces, the hydrate crusts formed with unconsumed gases

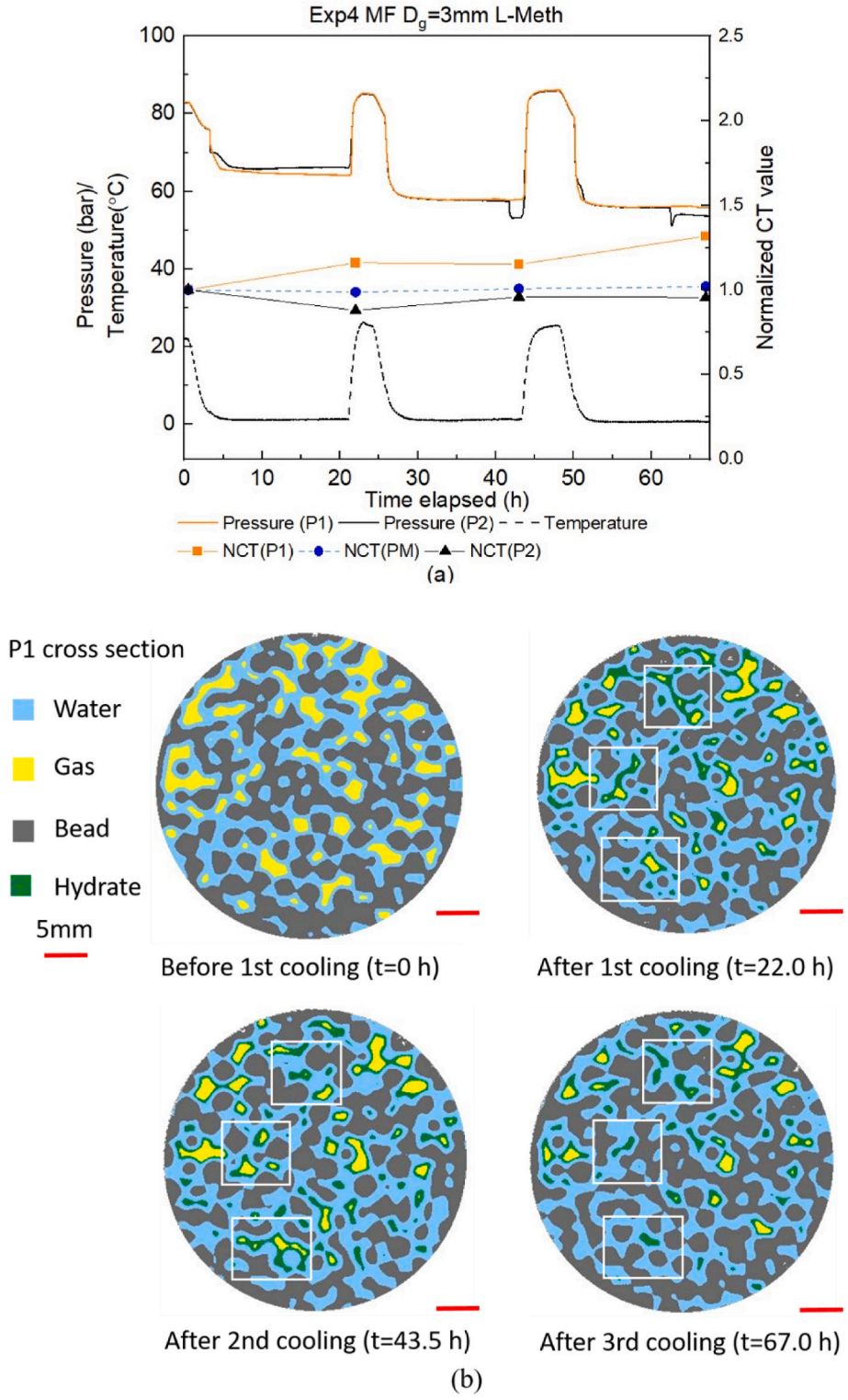

Fig. 8. Characteristics of CH_4/CO_2 hydrate formation during annealing process for 3000 ppm L-methionine at Exp4 (D_g = 3 mm): (a) variations of pressures, gas compositions and NCT values and, (b) 2D images at P1 cross-section for phase characterization. The hollow white rectangle is for comparison at the same positions.

that enclosed inside the formed hydrates. The remained gas could not be consumed because of lacking gas-water interfaces, which was owing to hydrates acting as barriers. The common characteristics of hydrate clusters and hydrate crusts were non-contact types surrounding glass beads. This phenomenon of hydrate formation was consistent with the descriptions of pore-filling hydrate types in references (Li et al., 2023; Yang et al., 2015). The similar gas-water-hydrate distributions during annealing process at P1 cross-section suggested a good repetition of hydrate formation during annealing process.

3.1.2. Hydrate formation patterns in L-methionine

Fig. 8 presents characteristics of CH_4/CO_2 hydrate formation with 3000 ppm L-methionine at Exp4. L-methionine can accelerate hydrate formation kinetics by promoting hydrate induction (Cai et al., 2017). However, it was found that no obvious reduction in induction time and the pressure drop (32.5 bar) in Exp4 was smaller than that (42.7 bar) in Exp2. This indicated that mass transfer dominated during hydrate formation. The lower hydrate formation kinetics in L-methionine may be attributed to fast promotor-driven CO_2 hydrate formation covering residual CH_4-rich gas and hindered further mixed hydrate formation. The same quick CO_2 hydrate layer formation and low methane hydrate reformation were reported in our previous works (Pandey et al., 2020a, 2020c). Meanwhile, there was no obvious pressure differential between P1 and P2 during annealing process at Exp4 of L-methionine. This was caused by larger diameter of glass bead ($D_g = 3$ mm) in Exp4 than that ($D_g = 2$ mm) in Exp1. Large particle size created larger pore size and better connectivity within core (Gong et al., 2020; Kashif et al., 2019).

Differently, NCT values at P1, PM and P2 presented different trends with time for 3000 ppm L-methionine at Exp4. It can be seen from Fig. 8 (a) that NCT (P1) showed an obvious increasing trend, NCT (PM) remained unchanged and NCT (P2) exhibited a small decreasing trend. The final NCT (P1) for L-methionine was 1.32 after annealing process, larger than that (1.06) for pure water, indicating more violent fluid migration with higher CT values, i.e. the area occupied by gas was replaced by water and hydrate due to gas consumption.

Fig. 8(b) exhibits 2D images of phase characterization at P1 cross-section. It can be observed that gas phase was dispersed in water phase just before 1st cooling (t = 0 h). Afterward, scattered hydrates appeared between boundaries of gas phase and water phase after 1st cooling (t = 22.0 h). Hydrate morphologies changed with annealing process, with the area of gas phase shrank. One reason was that multi-cooling improved gas-water distribution and thus increased gas dissolution (Wu et al., 2013). The other was that hydrate formation consumed more gas with cycles of cooling (Yin et al., 2019). This shrinkage of gas phase and replacement of water/hydrate phase increased CT values at P1 cross-section, which complied with the growth of NCT (P1) in Fig. 8 (a). And similar types of pore-filling hydrates including hydrate clusters and hydrate crusts, with or without gas enclosed in hydrate phase, appeared in Exp4 of 3000 ppm L-methionine. This indicated that gas dissolution in water or gas diffusion through hydrate crusts, rather than solution type, dominated the patterns of hydrate formation. This was further verified by the findings in (Kou et al., 2021).

The information on hydrate synthesis correlated with core properties of Exp 1-4 is summarized in Table 2. It can be seen that CH_4-rich hydrates (X > 1) formed after hydrate synthesis in Exp1-4. Both higher hydrate saturation (S_H) and CH_4 to CO_2 ratio in hydrate were achieved in Exp2 ($S_H = 12.5\%$ and X = 3.93) and Exp3 ($S_H = 12.2\%$ and X = 3.18) compared with that ($S_H = 7.1\%$ and X = 1.75) in Exp1, indicating more pure CH_4 or CH_4-rich hydrate formation in larger bead diameter ($D_g = 3$ mm and 5 mm) than that in small bead diameter ($D_g = 2$ mm). Hydrate saturation was consistent with those references describing larger particle size promoted higher hydrate saturation by increasing gas-water interface contact area (Lu et al., 2011; Pan et al., 2018). CH_4 to CO_2 ratio in hydrate (X) in different bead size was discussed as follow. The X was (1.37-1.45) for 70 mol%CH_4/CO_2 gas forming mixed hydrates calculated by CSMGem (Colorado School, 2015), because CO_2 hydrates have more moderate hydrate equilibrium conditions and thus lean CO_2 gas is more likely to enter into hydrate phase than rich CH_4 gas. However, the results of higher X and S_H in Exp2 and Exp3 indicated that more pure CH_4 or CH_4-rich hydrates generated. Note X was calculated from gas samples at P1. Thus, good pore connectivity along the sample in Exp2 and Exp3 could trigger more CH_4-rich hydrate formation and reflect pratical CH_4/CO_2 mole fraction in hydrate under favorable mass transfer. While the result of lower X and S_H in Exp1 indicated less amount of CH_4-rich hydrate systhesis that attibuted to poor pore connectivity, which might not reflect the actual hydrate fraction in sample under insufficient mass transfer. In addition, CO_2 mole fraction of 43.0% in CH_4/CO_2 hydrates (i.e. X = 1.33) in Exp4 was the highest. This confirmed the promotion effect of L-methionine was mainly on CO_2 hydrate storage despite lower S_H was caused by high-speed CO_2 hydrate formation hindering CH_4-rich hydrate systhesis.

Promoting effect of L-methionine on mixed hydrate formation was absent in Exp4 compared with Exp1 according to hydrate saturation and final CT values. The absence of promoting effect can be ascribed to two reasons. One was that hydrate formation in these artificial cores was dominated by mass transfer (gas-water interface and pore connectivity). The other was that localized heterogeneous hydrate generated in cores affected local CT values at a specific cross-section. Mass transfer and localized heterogeneity caused higher hydrate saturation in Exp2 with water than that in Exp4 with L-methionine. This observation was consistent with the assumption proposed by (Li et al., 2014) that mass transfer was the key factor controlling hydrate formation. Hence, CT values were restricted to a specific cross-section of HBS. For Exp2 and Exp3 in water-saturated cores with similar hydrate saturation, final average NCT value for Exp2 (1.04) was larger than that for Exp3 (0.99). It can be identified that NCT values were more correlated with fluid and hydrate distribution than saturation. This can be explained in Fig. 9 of phase characterization at three cross-sections after hydrate formation. Note that larger areas of continuous gas phase existed at P2 cross-section in Exp3, and this gas phase had no contribution to NCT values. Collectively, a more homogeneous distribution of gas-water-hydrate was achieved in Exp2 ($D_g = 3$ mm) compared with that in Exp3 ($D_g = 5$ mm).

3.2. Characteristics of CH_4/CO_2 hydrates during depressurization

Multistep depressurization (MD) was conducted after synthesis of artificial hydrate-bearing cores. Scheme of 8–15 bar pressure drops and 4-hour shut-in period was employed to dissociate CH_4/CO_2 hydrates. The parameters of depletion operations are summarized in Table 3. The influences of different bead diameters and solutions on MD were

Table 2
Summary of CH_4/CO_2 hydrate formation parameters in Exp1-4. D_g is diameter of beads. X is CH_4 to CO_2 ratio in mole amount in hydrate. X_{CSM} is the value of X calcuated from software CSMGem (Colorado School, 2015). NCT is normalized CT value, and the initial NCT is 1.00 before hydrate formation.

No.	D_g (mm)	Solution	Residual water saturation (%)	Hydrate saturation (%)	X	X_{CSM}	Final NCT at P1/PM/P2	Average final NCT
Exp1	2	Water	45.8	7.1	1.75	1.37	0.98/0.99/1.00	0.99
Exp2	3	Water	42.2	12.5	3.93	1.39	1.19/0.96/0.97	1.04
Exp3	5	Water	43.1	12.2	3.18	1.45	1.12/1.02/0.84	0.99
Exp4	3	L-meth	46.4	7.7	1.33	1.39	1.32/1.02/0.96	1.10

The concentration of L-methionine (L-meth) is 3000 ppm.

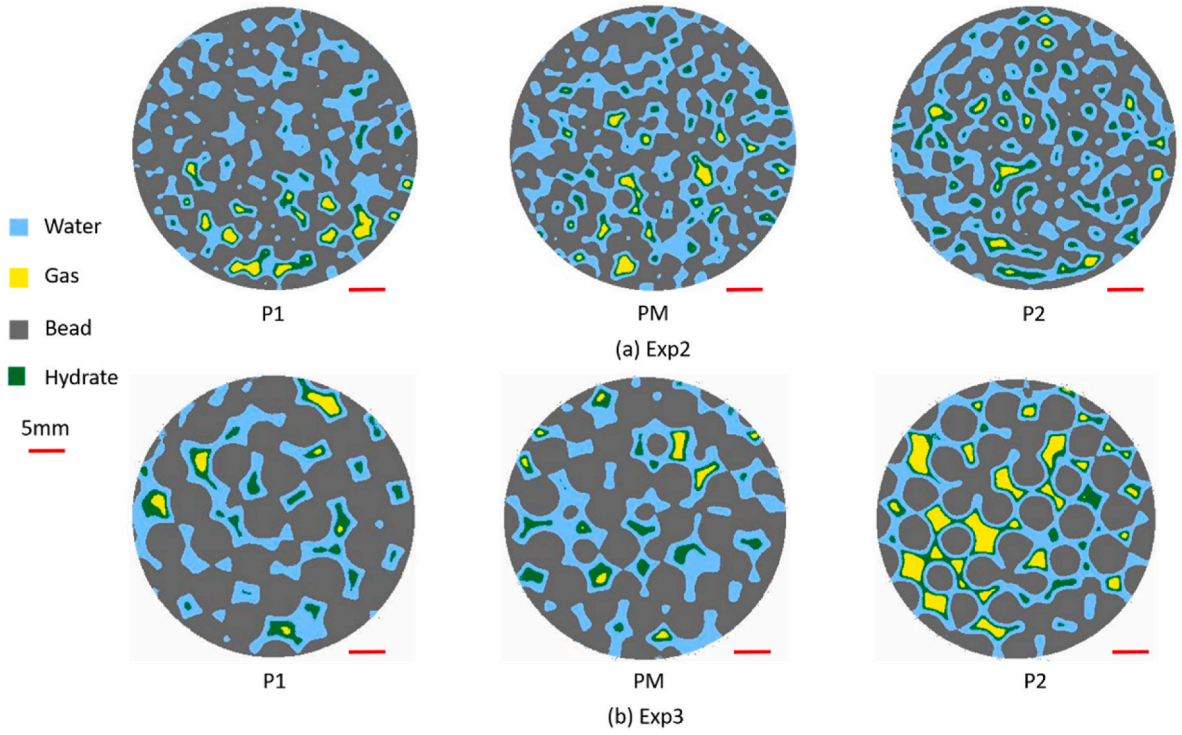

Fig. 9. 2D images of phase characterization at P1, PM and P2 after hydrate formation: (a) Exp2 (D_g = 3 mm), and (b) Exp3 (D_g = 5 mm).

Table 3
Summary of operation parameters for MD at Exp1-4.

No.	D_g (mm)	Solution	Hydrate saturation (%)	Staring pressure (bar)	Ceasing pressure (bar)	Average core temperature (°C)	Steps of depletion
Exp1	2	Water	7.1	59.4	21.2	0.80	8
Exp2	3	Water	12.5	41.9	21.7	1.33	10
Exp3	5	Water	12.2	29.3	8.5	0.45	8
Exp4	3	L-meth	7.7	53.6	20.4	0.60	9

evaluated.

To characterize phase changes just before and after depletion as well as during shut-in period, variations of pressure-temperature and NCT values during MD were combined with CT images at selected critical points in Exp1, as exhibited in Fig. 10. Staged pressures occurred at P1 as proceeding of depletion whereas pressures kept unchanged at P2 throughout MD. This was caused by gas release conducted at P1, whereas hydrate blockage within core caused pressure differential. Thus, the depletion pressure is referred to as the pressure at P1 and the NCT value is referred to as NCT (P1) in the following text.

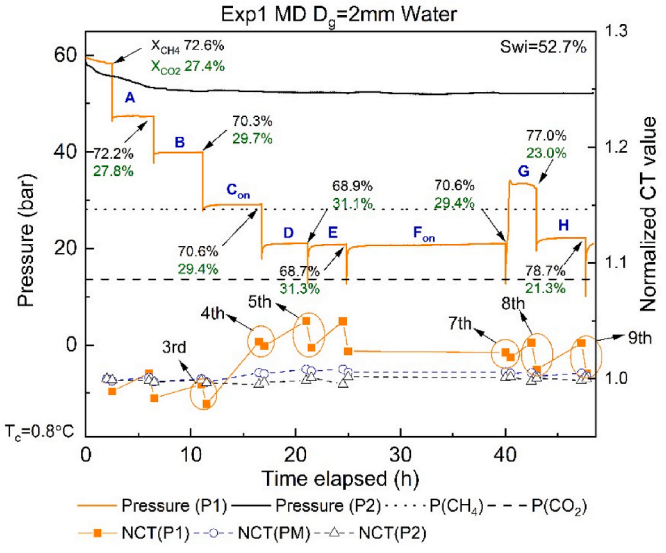

Fig. 10. Variations of pressures, gas compositions and NCT values of CH_4/CO_2 hydrate dissociation during MD for pure water at Exp1 (D_g = 2 mm).

Note a sudden large growth of NCT emerged during Stage C. This resulted from increased area of water phase caused by gas-water migration at P1 cross-section, as shown in Fig. 11(a–b), because depletion pressures were above CH_4 hydrate stability pressure (PCH_4) without hydrate dissociation producing water. After depletion pressures were reduced between PCH_4 and CO_2 hydrate stability pressure (PCO_2), apparent pressure rebounds happened and they were attributed to hydrate dissociation after Stage C. The dissociating gas and water redistributed inside pores as shown in Fig. 11(b–c), and the enlarged water phase caused second increase of NCT during Stage D. When depletion pressures touched PCO_2 at final Stage D and Stage E, more violent pressure rebounds occurred and the pressures could recover to previous levels before depletion. Yang et al. (2021) reported a gradual converting control mechanism of hydrate dissociation from kinetics-limitation to diffusion-limitation. The pressure rebounds and full pressure recoveries verified that the hydrate dissociation was dominated by hydrate kinetics with sufficient heat and mass transfer in this scenario. The recovered NCT values at final Stage E were as same as that at final Stage D, which further supported the kinetics-dominated mechanism above.

Afterward, an unexpected pressure rebound to a higher value at final Stage F. This phenomenon of recovering pressure higher than depletion

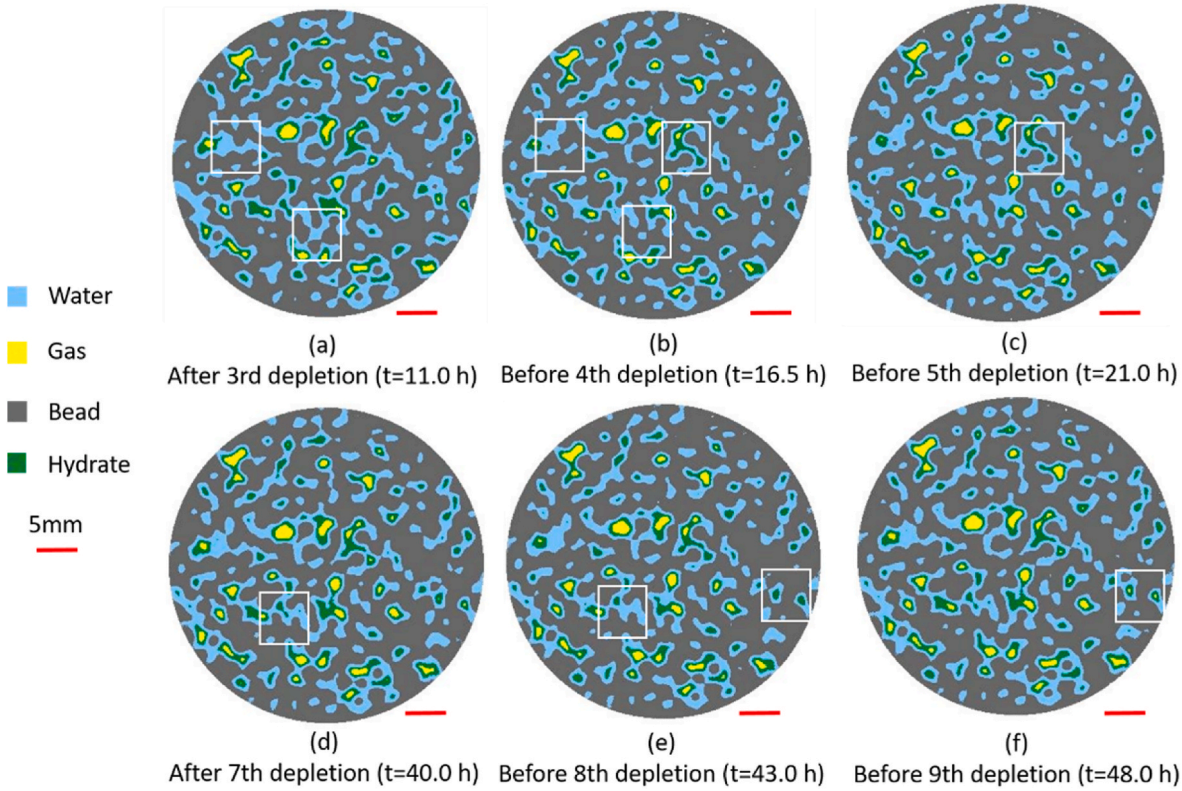

Fig. 11. 2D images of phase characterization for P1 cross-section at selected point-in-time of Exp1 (D_g = 2 mm). The hollow white rectangles are for comparison at same positions.

pressure was absent in our previous studies (Ouyang et al., 2022a, 2022b; Pandey et al., 2022b). This resultant pressure profile indicated that pressure release from dissociation is dominating instead of pressure reduction on account of reformation. It may be possible that no major reformation occurred and system experienced rapid dissociation. In previous instantons of pressure depletion, rapid dissociation followed by rapid reformation thus pressure rebound was compensated by pressure loss due to reformation. Major dissociation without reformation could occur due to absence of any driving force for CO_2-rich hydrate reformation. Two reasons accounted for absence of driving force: (1) dissociation below PCO_2 dissociated additional CH_4-rich mixed hydrates. This caused increase of CH_4 gaseous mole fraction (XCH_4) thus lower CO_2 gaseous mole fraction, delaying CO_2-rich hydrate reformation; (2) longer induction time for reformation was needed. It was possible that 4 hours may not be sufficient for CO_2-rich hydrate reformation. Also, these pressure rebounds were generally observed in those cases when system pressures were decreased closer to PCO_2, supporting occurrences of CO_2-rich hydrate dissociation. This was further supported by hydrate phase decrease and water phase increase in Fig. 11(d–f).

3.2.1. *Influence of bead diameter on multistep depressurization*

Diameter of beads has a direct relationship with core properties such as pore size and pore volume, and pore properties therefore influenced hydrate dissociation by affecting equilibrium pressures (Uchida et al., 2002), capillary pressures (Misyura, 2016), gas-water flow behaviors (Misyura, 2016) and gas-water-hydrate distribution (Yin et al., 2016). Fig. 12 presents pressures, gas compositions and NCT values of CH_4/CO_2 hydrate dissociation during MD for pure water at Exp2 (D_g = 3 mm). Stepped depletions caused staged pressure drops at P1 and no pressure reduction at P2. This pressure differential existed from Stage A till Stage I. It can be observed that small pressure growths appeared when depletion pressures were between PCH_4 and PCO_2, with XCH_4 increased to 65.5 mol% at final Stage C. These two patterns were attributed to

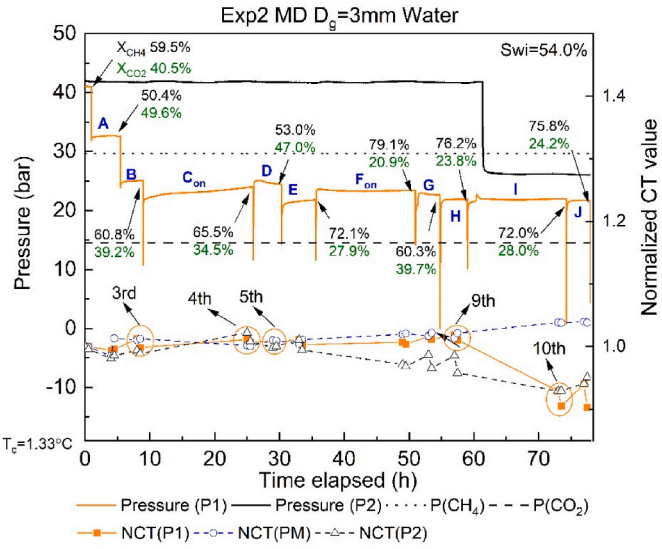

Fig. 12. Variations of pressures, gas compositions and NCT values of CH_4/CO_2 hydrate dissociation during multistep depressurization for pure water at Exp2 (D_g = 3 mm).

CH_4-rich hydrate dissociation, i.e. 79.7 mol% CH_4/CO_2 hydrates after hydrate formation in Exp2. Comparably, slight pressure reductions emerged as well during Stage D. The XCH_4 inversely decreased to 53.0 mol%. These two patterns were caused by CH_4-rich hydrate reformation. Unchanged pressure with XCH_4 variations indicated both hydrate reformation and dissociation existed during shut-in period. Nevertheless, such hydrate dissociation and reformation were repeated in the following stages until a sudden significant pressure drop happened at

P2. Note that NCT at three cross-sections remained constant at around 1.00 before obvious pressure relief during Stage I. This indicated that only gas was produced from hydrate without water production during these depletions. After apparent pressure drop at P1 during Stage I, NCT (P1) and NCT (P2) decreased largely without pressure variations during shut-in period, indicating gas migration between P1 and P2; whereas NCT (PM) jumped to 1.04, indicating water migration in middle pore.

Fig. 13 presents the 2D images of phase distribution at P1 cross-section during CH_4/CO_2 hydrate dissociation for pure water at Exp2 ($D_g = 3$ mm). It can be seen from Fig. 13(a–b) that hydrate phase became smaller and gas phase enlarged in the hollow white rectangle, indicating hydrate dissociation at Stage B. And it was seen from Fig. 13(b–c) that hydrate phase became larger and gas phase shrank, indicating hydrate reformation during Stage D. These characteristics complied with the observations in NCT values above. According to Fig. 13(d–f), concurrent hydrate dissociation and reformation appeared in different areas of P1 cross-section during Stage I. Combined with decrease of NCT (P1) and NCT (P2) whilst increase of NCT (PM), it was denoted from Fig. 13(d–f) after pressure relief during Stage I that massive hydrates dissociated at middle of core, and the dissociating gas moved from the middle towards P1 and P2.

The patterns of pressures and NCT values during MD for pure water at Exp3 ($D_p = 5$ mm) were presented in Fig. 14. The pressure rebounds immediately appeared after 1st depletion together with XCH_4 increased to 65.1 mol% at the end of Stage B, indicating CH_4-rich hydrate dissociation at pressure between PCH_4 and PCO_2. Afterward, XCH_4 dropped gradually when depletion pressure touched PCO_2. The sudden growth of XCH_4 during Stage G may be attributed to heterogeneous CH_4 gas and CO_2 gas distribution within pore. Note pressure at P2 was simultaneously equal to that at P1 until Stage H. This suggested good connectivity during MD for larger size diameter (5 mm) of beads.

The responses of NCT in Exp3 of larger diameter beads ($D_g = 5$ mm) were different from those in Exp1 and Exp2 of smaller diameter beads ($D_g = 2$ mm and $D_g = 3$ mm). The overall NCT values were below 1.0

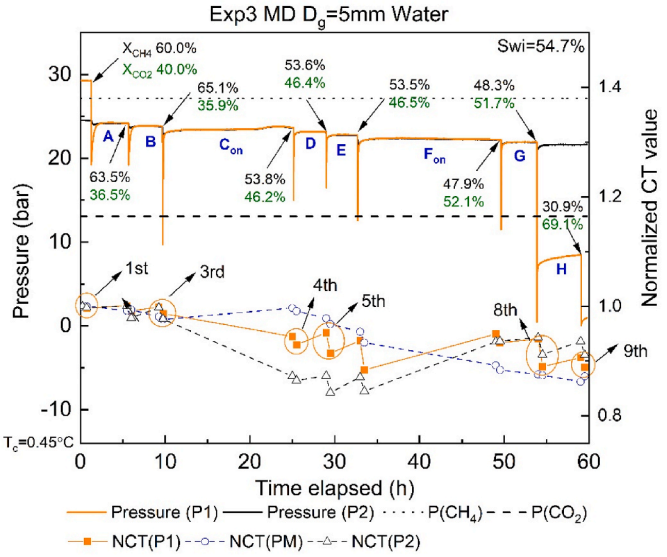

Fig. 14. Variations of pressures, gas compositions and NCT values of CH_4/CO_2 hydrate dissociation during multistep depressurization for pure water at Exp3 ($D_g = 5$ mm).

throughout MD, indicating that hydrate reformation dominated or more gas-water migrated and distributed in these three cross-sections after MD. Due to no obvious pressure drops observed during shut-in period, the inhibition of NCT was attributed to gas-water redistribution. This was further supported by NCT (P1) and NCT (P2) decrease whist NCT (PM) increase during Stage C, indicating gas-water migrated from the middle of core towards P1 and P2. Inverse fluid migration was noticed during Stage F at which NCT (P1) and NCT (P2) increased whist NCT (PM) decreased, i.e. water moved towards P1 and P2 while gas

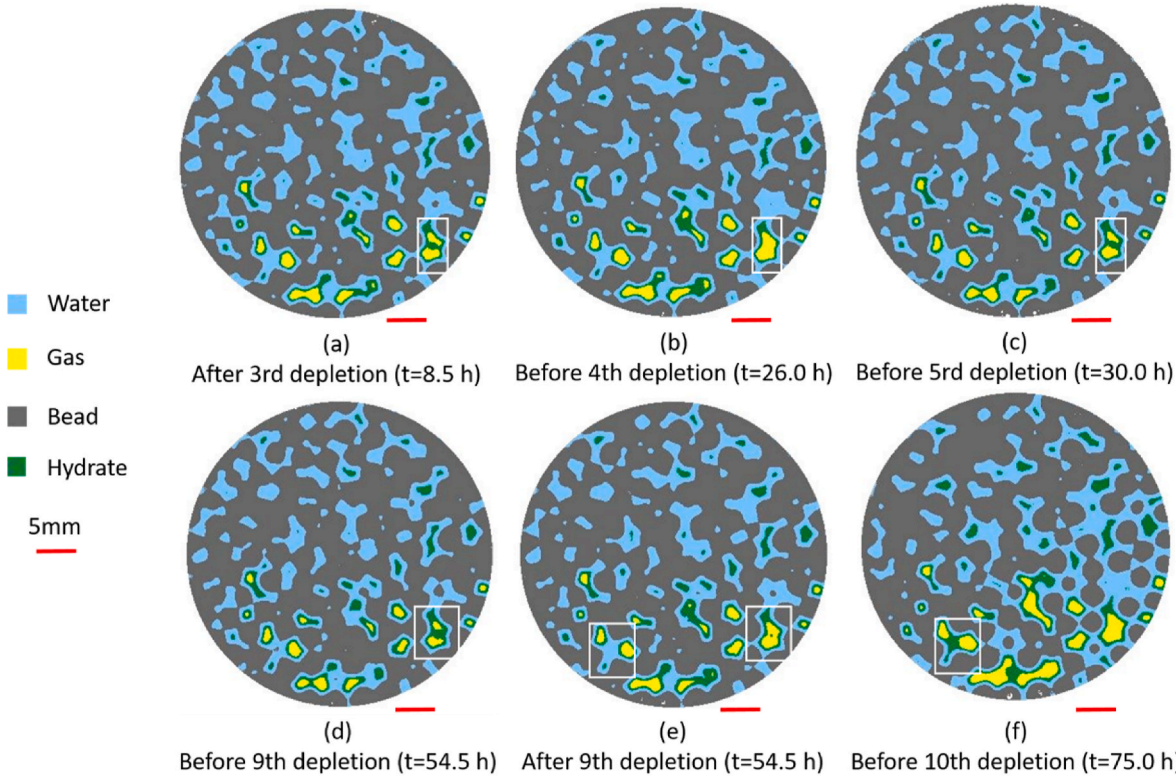

Fig. 13. 2D images of phase characterization for P1 cross-section at selected point-in-time in Exp2 ($D_g = 3$ mm). The hollow white rectangles are for comparison at same positions.

accumulated around the middle.

Phase characterization showed the enlargement and shrinkage of phases at P1 cross-section for selected point-in-time in Exp3 (D_g = 5 mm) in Fig. 15. It was seen from Fig. 15(a–c) that gas phase enlarged during Stage A and Stage B, with NCT values remained close to 1.00. Combined with XCH_4 growth mentioned above, this indicated CH_4-rich hydrate dissociation without much water production. According to Fig. 15(b–c), hydrate phase enlarged during Stage C while gas phase shrank with NCT values reduced to 0.94. Combined with XCH_4 reduction exhibition without pressure drop during Stage C, this identified partial re-distribution of CH_4 gas and CO_2 gas, water and hydrate instead of CO_2-rich hydrate reformation. Similar observations were repeated for Fig. 15(c–d) and the corresponding NCT values were decreasing and increasing. However, no obvious pressure variations denoted that these changes in phases and CT values were mainly correlated with fluid migration and distribution rather than massive hydrate dissociation and reformation during Stage D-F. Comparably, apparent gas phase enlargement in Fig. 15(e–f) together with NCT value decreases were mainly connected with hydrate reformation as pressure rebounds appearing during Stage H. And the dissociating hydrates were determined as CO_2-rich based on obvious decreases of XCH_4.

Fig. 16 summarizes the variations of XCH_4, CH_4 recovery percentage (RCH_4) and CO_2 storage ratio (SCO_2) with depletion pressure during MD in Exp1-4 with different diameters of glass beads. Note P_{end} was the ending point at which stepped depletion should be terminated. As shown in Fig. 16(a–c), XCH_4 for Exp1 and Exp2 were enhanced through stepped depletion. The highest XCH_4 reached 78.7 mol% and 79.1 mol% for Exp1 and Exp2 at the ending point. XCH_4 for Exp3 was, however, inhibited after stepped depletion and only 53.5 mol% at the ending point, at which RCH_4 (78.2%) was slightly higher than those (74.4% and 73.1%) for Exp1 and Exp2, but SCO_2 (55.7%) was much lower than those (83.8% and 83.4%) correspondingly. The data above illustrated that hydrate-bearing sediments with glass beads of higher diameters (D_g = 5 mm) presented low efficiency of dissociation parameters.

The influences of bead diameter on CH_4/CO_2 hydrates during MD were analyzed. A smaller diameter of 2 mm caused pressure differential across whole process of MD, while a mediate diameter of 3 mm generated pressure relief during shut-in period and a larger diameter of 5 mm only had pressure differential at the end of MD. On the one hand, smaller size of sand particles may form HBS of low permeability that was unbeneficial to fluid mobilization. Given the beads in this work were water-wet, gas tended to occupy larger pore spaces (Waite et al., 2009). Thus, larger size of beads may have larger pore spaces and higher permeability that favors gas production. It was noted from phase characterization that the hydrate type in this work was pore-filling with a weak hydrate cementation effect. The mechanical strength of hydrate-bearing sediments was larger for host sediments with larger size sands due to stronger friction force and hydrate cement (Luo et al., 2018; Miyazaki et al., 2010), providing more guarantee for safe exploitation of hydrate. In contrast, exploitation of hydrates in sediments with smaller sizes of sands had more chances of suffering skeleton failures of reservoir and sand production (Wu et al., 2021). To sum up, effective and safe fluid production in reservoirs needs full consideration of particle size of specific type of sediment and exploitation scheme designs. An enhanced technique e.g. thermal simulation could be coupled to dissociate the blocking hydrates to promote gas-water flow behaviors in HBS with smaller particle size, or to facilitate low efficiencies of hydrate dissociation parameters in HBS with larger particle size.

3.2.2. *Influence of L-methionine on multistep depressurization*

Amino acids are environmentally friendly and effective kinetic promotors influencing water chemistry/activity and thus affecting hydrate formation kinetics. L-methionine is a hydrophobic amino acid that improves CO_2 hydrate storage effectively at appropriate concentrations (Cai et al., 2017; Liu et al., 2022). Our previous studies proved that L-methionine showed higher gas uptake and lower induction time for hydrate formation and effectively assisted CH_4–CO_2 swapping for high CO_2 storage, and the highest performances were obtained with

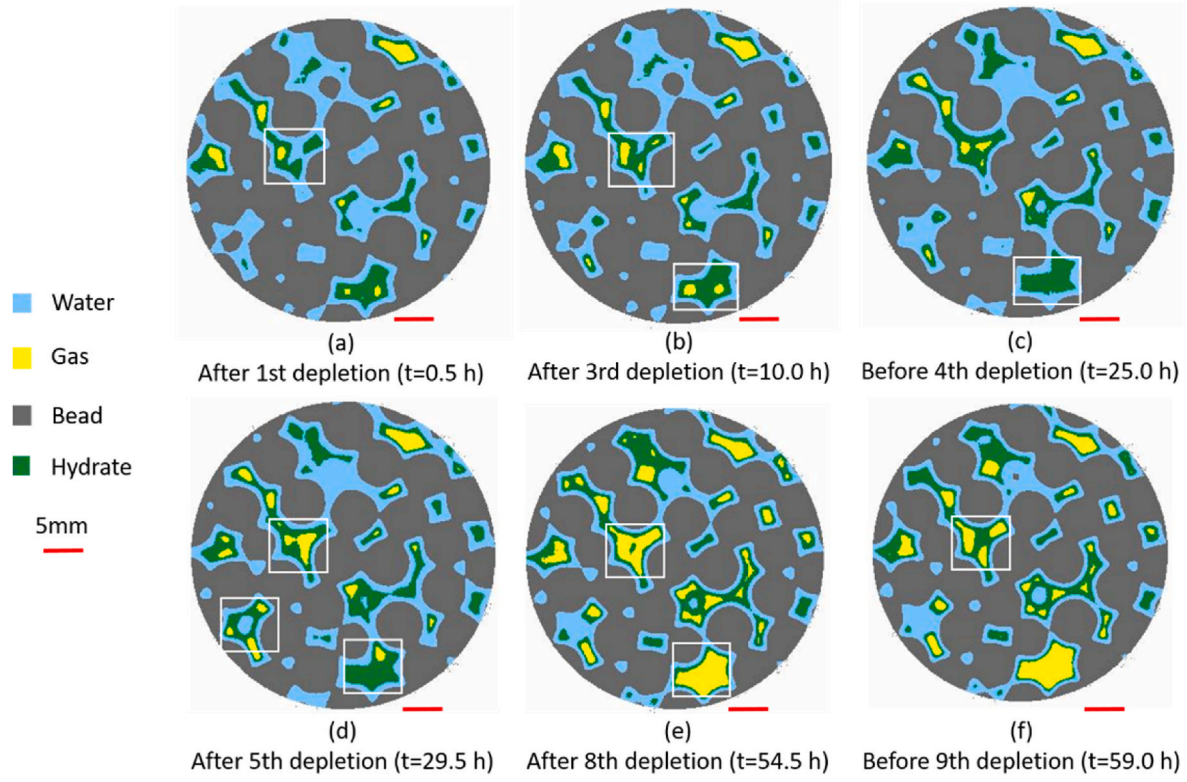

Fig. 15. 2D images of phase characterization for P1 cross-section at selected point-in-time in Exp3 (D_g = 5 mm). The hollow white rectangles are for comparison at same positions.

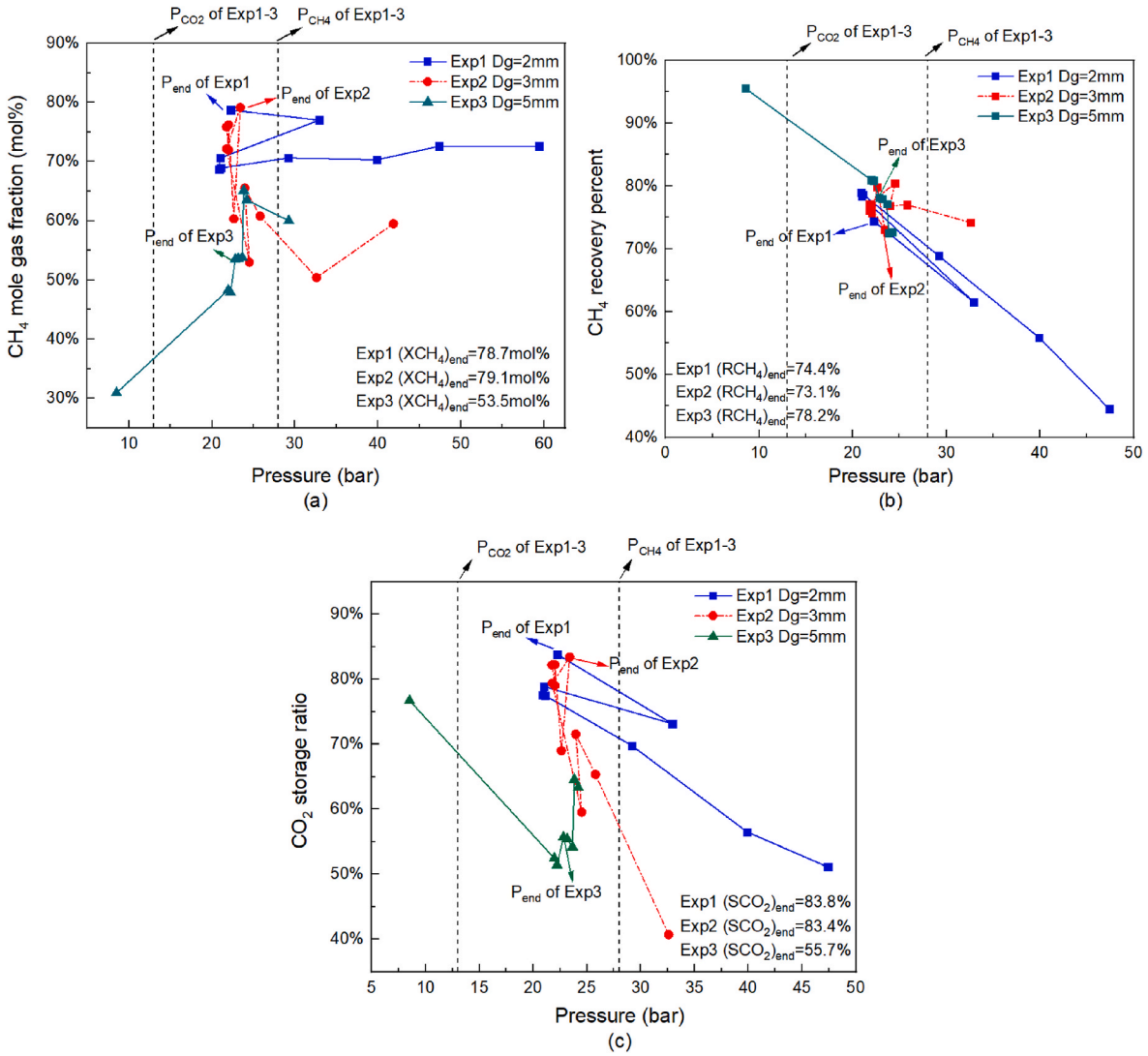

Fig. 16. Summary of dissociation parameters during MD in Exp1-3 of different diameters glass beads: (a) XCH_4 with depletion pressure; (b) CH_4 recovery percentage (RCH_4) with depletion pressure and, (c) CO_2 storage ratio (SCO_2) with depletion pressure.

L-methionine of 3000 ppm (Pandey et al., 2020b, 2021b). Thus, L-methionine of 3000 ppm was employed in this work to study dissociation characteristics during MD after CH_4–CO_2 swapping.

Fig. 17 presents the patterns of pressures, temperatures and NCT values for CH_4/CO_2 hydrate dissociation during MD in Exp4 with L-methionine. Gas compositions showed no apparent variations with stepped depletions until Stage F. Thus, varying NCT values were attributed to fluid migration within core affecting phase distribution at specific cross-section. Stage F witnessed a continuous pressure rebound and a growth of XCH_4, denoting massive CH_4-rich hydrate dissociation with depletion pressure below PCH_4 but above PCO_2. Sudden drops of both NCT (P1) and NCT (P2) during Stage F also ascertained a large amount of gas release and gas accumulation at two ends of core. After Stage F, pressure rebounds and XCH_4 reductions supported occurrences of CO_2-rich hydrate dissociation at depletion pressures below PCO_2.

Profiles of phase characterization for P1 cross-section at selected point-in-time in Exp4 with L-methionine are shown in Fig. 18. Only slight differences of gas phases were seen in Fig. 18(a–c), supporting the explanation of fluid migration aforementioned affecting pressures, gas compositions and NCT values. However, no more changes in phases were detected in Fig. 18(d–f). This was inconsistent with the description above in pressures, gas compositions and NCT values. This inconsistency may be caused by heterogeneity within core. The combined indication of

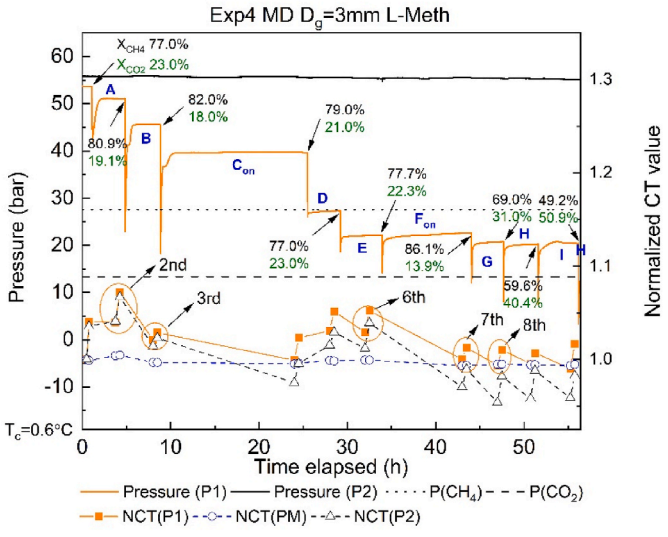

Fig. 17. Variations of pressures, gas compositions and NCT values of CH_4/CO_2 hydrate dissociation during multistep depressurization for L-methionine at Exp4 (D_g = 3 mm).

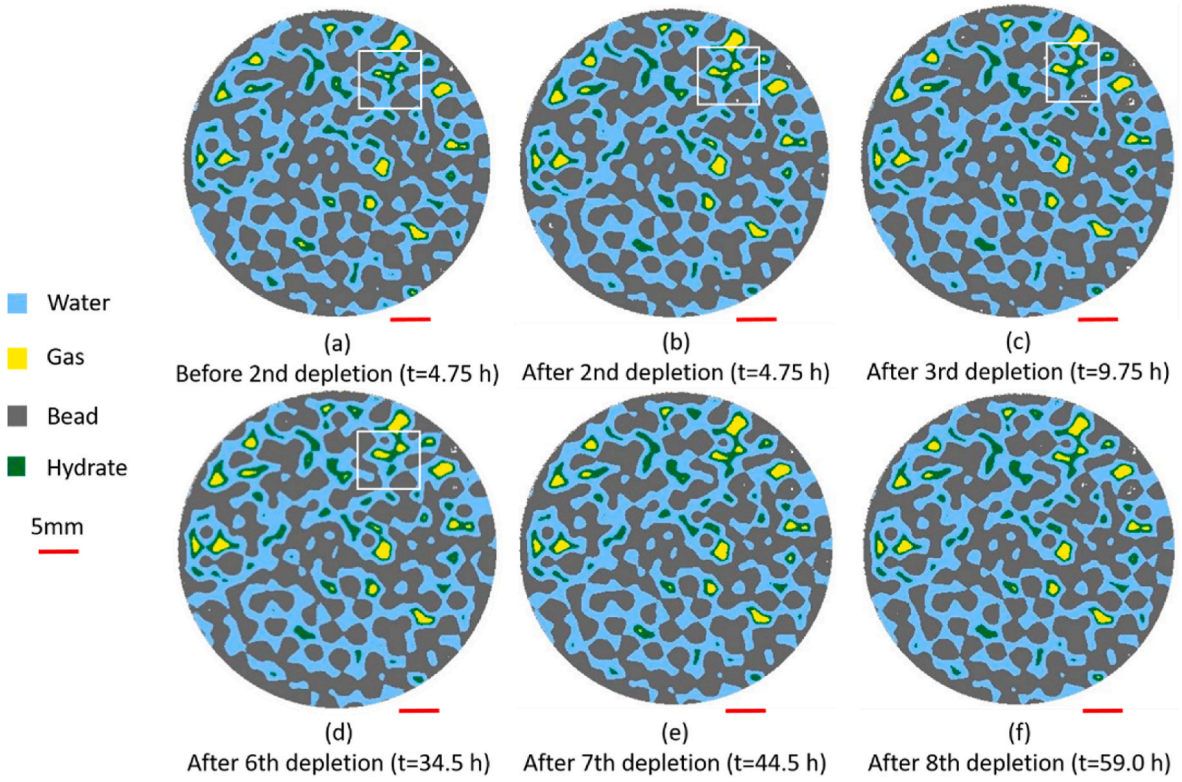

Fig. 18. 2D images of phase characterization for P1 cross-section at selected point-in-time in Exp4 with L-methionine (D_g = 3 mm). The hollow white rectangles are for comparison at the same position.

pressure and gas compositions elucidated CO_2-rich hydrates dissociated at one side of core even though blockage may prevent mass transfer at other side. However, the CT images were only concerned with one slice of a cross-section of core. Hence, inconsistency of hydrate dissociation existed and real scenario complied with the overall responses of pressure and XCH_4 rather than the localized features of CT images.

The influence of L-methionine could be determined in Fig. 19 of summarized dissociation parameters during MD in Exp2 and Exp4. In Fig. 19(a), XCH_4 in water was below that in L-methionine throughout MD. This was mainly caused by promoted CO_2 storage before MD, e.g. SCO_2 of 61.4% with L-methionine compared with 40.7% without L-methionine (boosted by 20.7%). This brought a relatively high initial XCH_4 of 77.0 mol% with L-methionine compared with 59.5 mol% without L-methionine (boosted by 17.5 mol%). However, this promoting effect on CO_2 storage became weak during MD in Exp4 with SCO_2 enhanced from 61.4% to the highest 88.8% in Fig. 19(c). One reason may be that mass transfer was hindered in Exp4 with continuous pressure differential i.e. hydrate blockage existed throughout MD. And no massive hydrate dissociation and reformation were observed in Exp4 according to mixed hydrate characteristics with time. In contrast, improved CO_2 storage was notable in Exp2 of water with SCO_2 increased from 40.7% to the highest 83.4% in Fig. 19(c), with apparent pressure rebounds and declines as well as sudden pressure relief during shut-in period. In terms of CH_4 production, it can be seen from Fig. 19(b) that RCH_4 increased with depletion pressure decreased in Exp2 and Exp4. Comparably, RCH_4 in Exp4 was lower than that in Exp2 after depletion pressures reduced just below PCH_4, and the former exceeded the latter at depletion pressure of 20 bar. This suggested that L-methionine could significantly boost CH_4 production at pressures between PCH_4 and PCO_2 because it highly helped CO_2 hydrate storage. This was consistent with the enhancement of L-methionine on hydrate formation in CH_4–CO_2 gas mixture systems (Prasad and Kiran, 2020; Prasad and Sai Kiran, 2018). Moreover, the mechanism behind enhanced CO_2 hydrate storage was that L-methionine acted as a surfactant and reduced surface tension between gas phase and water phase, promoting gas molecules to diffuse into water for hydrate nucleation (Cai et al., 2017; Raza et al., 2019). It was also concluded that CH_4 recovery was beneficial from depletions of mixed gas with higher XCH_4 and thus Exp4 of L-methionine outperformed Exp2 of water.

3.3. Comparison of CH_4 recovery and CO_2 storage

Table 4 summarizes the production parameters at suggested ending point of MD. It can be seen that at a similar suggested ending point, higher XCH_4 (78.7 mol%/79.1 mol%) and SCO_2 (83.8%/83.4%) were obtained in smaller bead diameters (D_g = 2 mm/3 mm), compared with those (XCH_4=53.5 mol% and SCO_2=55.7%) in larger bead diameter (D_g=5 mm) This indicated unconsolidated sediments with smaller particles were more beneficial to CH_4 gas recovery and CO_2 storage. L-methionine further improved production performances of XCH_4 and SCO_2 by effectively enhancing CO_2 hydrate storage in terms of both maximum XCH_4=86.1 mol% and SCO_2=88.8% in Exp4. Fig. 20 compared the XCH_4 and SCO_2 in this work with those in previous studies of unconsolidated sediment of CH_4-rich hydrates. It was seen in Fig. 20 that lower efficiencies of CH_4 recovery (XCH_4 = 76.8–81.3%) and CO_2 storage (SCO_2 = 82.5–85.3%) were obtained in natural sandstone because it is consolidated type of sediment. This type of sediment had the lowest efficiency of mass transfer compared with unconsolidated loose sand and unconsolidated artificial core. The particle size of unconsolidated loose sand was 0.9–1.6 mm while that of unconsolidated artificial core was 2/3 mm. It seemed that production parameters (XCH_4 = 74.9–79.1% and SCO_2 = 83.4–88.2%) in loose sand with the highest efficiency of mass transfer didn't obtain much higher performances compared with those (XCH_4 = 78.7–86.1% and SCO_2 = 83.4–88.8%) in aritificial core with mediate efficiency of mass transfer. This was because the surface properties of loose sand and artificial core were the other critical parameters affecting CH_4 productivity and CO_2 storage. Furthermore, chemical promotor (e.g. L-methionine) affecting pore

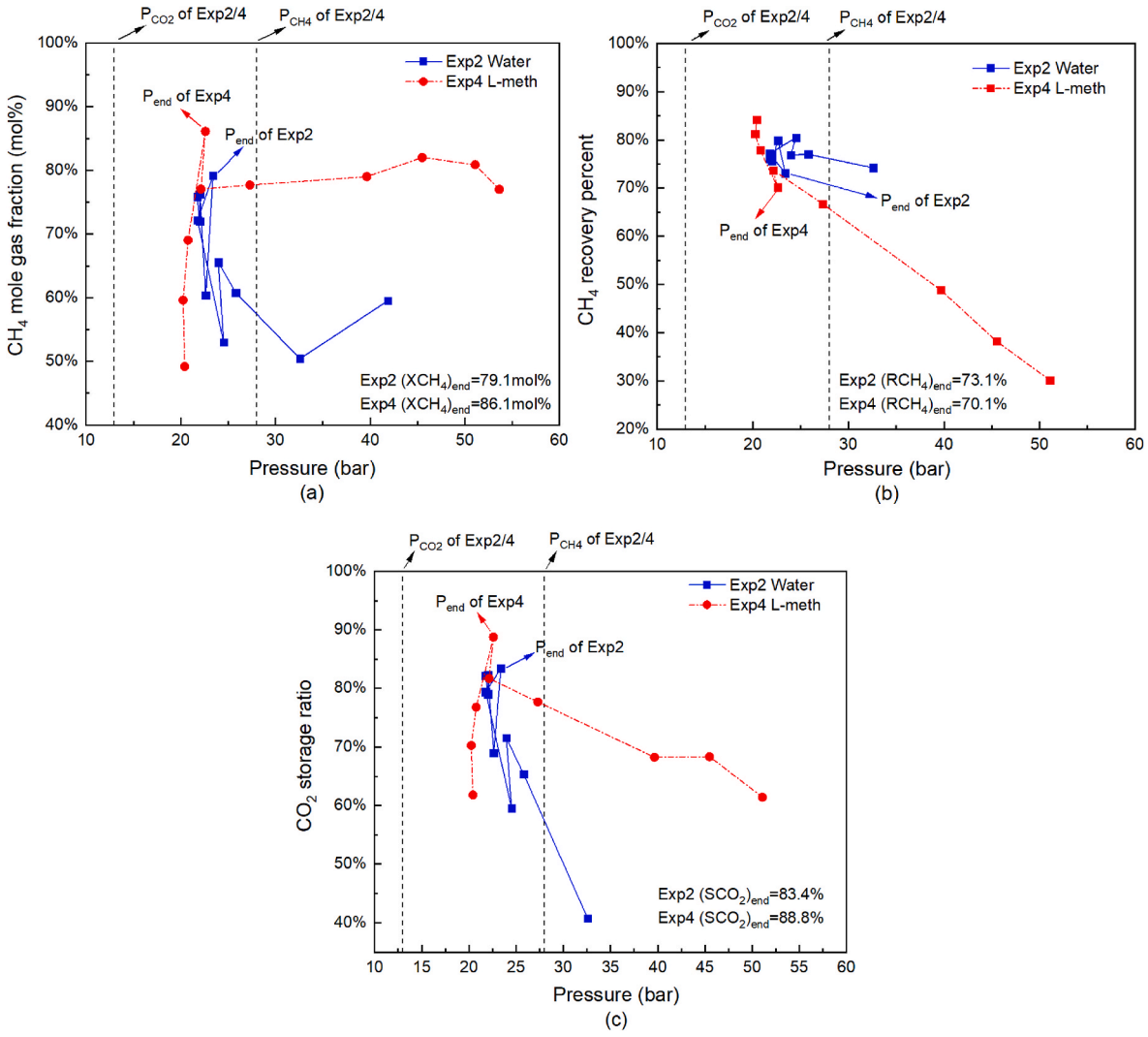

Fig. 19. Summary of dissociation parameters during MD in Exp2 of water and Exp4 of 3000 ppm L-methionine: (a) XCH_4 with depletion pressure; (b) RCH_4 with depletion pressure and, (c) SCO_2 with depletion pressure.

Table 4
Summary of production parameters for MD at the suggested ending point of Exp1-4. XCH_4 is CH_4 gaseous mole fraction. RCH_4 is CH_4 recovery percent. SCO_2 is CO_2 storage ratio.

No.	D_g (mm)	Solution	Suggested ending point (bar)	XCH_4 (mol%)	RCH_4 (%)	SCO_2 (%)
Exp 1	2	Water	22.3	78.7	74.4	83.8
Exp 2	3	Water	23.4	79.1	73.1	83.4
Exp 3	5	Water	22.8	53.5	78.2	55.7
Exp 4	3	L-meth	22.6	86.1	70.1	88.8

water chemistry can enhance mass transfer during MD for more CO_2 hydrate formation and thus boosting CO_2 storage with the highest XCH_4 and SCO_2 among these scenarios.

The characteristics of CH_4/CO_2 hydrate variation during MD can be divided into five types that were identified comprehensively by pressure responses, gas compositions and NCT values, as summarized in Fig. 21. When depletion pressures at P1 were reduced just below PCH_4, CH_4-rich hydrate dissociation was detected with pressure rebounds and increases of XCH_4. When pressures were further reduced between PCH_4 and PCO_2, CO_2-rich hydrate reformation was observed with pressure declines and decreases of XCH_4. It was noticed that NCT values showed an unobvious change because CT values of hydrate and water were not largely different (Jin et al., 2004, 2006; Sato et al., 2005). These two characteristics of CH_4/CO_2 hydrate dissociation and reformation during MD favored CH_4 recovery and CO_2 storage, as similar observed in our previous works of multistep depressurization (Ouyang et al., 2022a, 2022b; Pandey et al., 2022b) and in other references of slow stepwise depressurization (Phillips et al., 2019) and intermittent depressurization (He et al., 2022). However, when depletions were conducted at pressures above PCH_4, CH_4-rich hydrate reformation occurred with slight pressure reductions and decreases of XCH_4. And when depletions were performed at pressures below PCO_2, CO_2-rich hydrate dissociation emerged with remarkable pressure rebounds and decreases of XCH_4. It was also noted that NCT showed only small variations because of hydrate-water conversion. These two patterns of CH_4/CO_2 hydrate dissociation and reformation during MD were, however, unbeneficial to CH_4 recovery and CO_2 storage. It was therefore suggested that depletion pressures should be controlled between PCH_4 and PCO_2. In addition, greatly varying NCT values from below 1.00 to above 1.00 without varying CH_4/CO_2 gas fraction indicated gas-water migration and redistribution of gas-water-hydrate from P1 cross-section to somewhere else within core. This scenario to the benefit of CH_4 recovery and CO_2 storage was

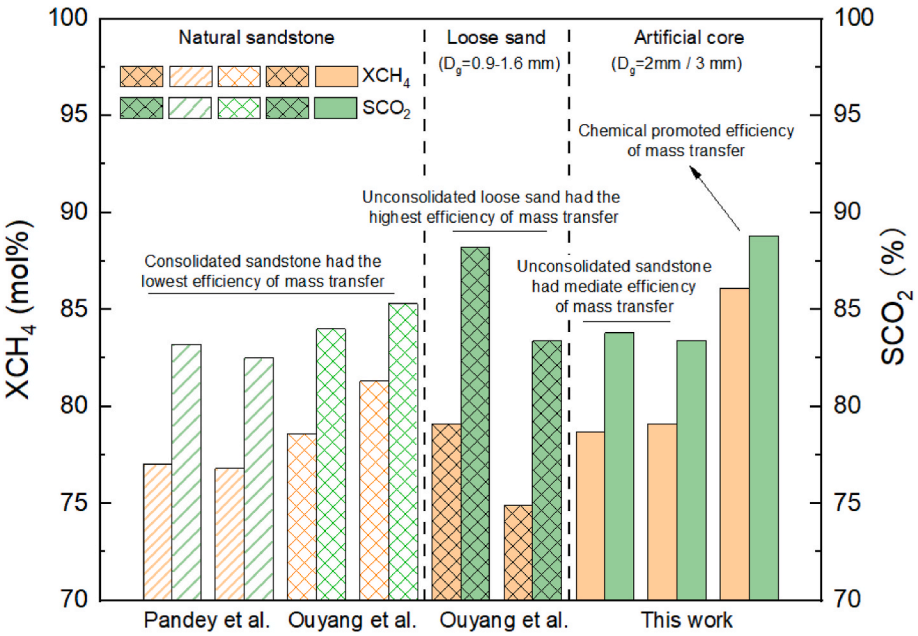

Fig. 20. Comparison of XCH_4 and SCO_2 in this work of artificial core and those in previous work of natural sandstone and loose sand (Ouyang et al., 2022a,b; Pandey et al., 2022b). More information is provided in Table B1.

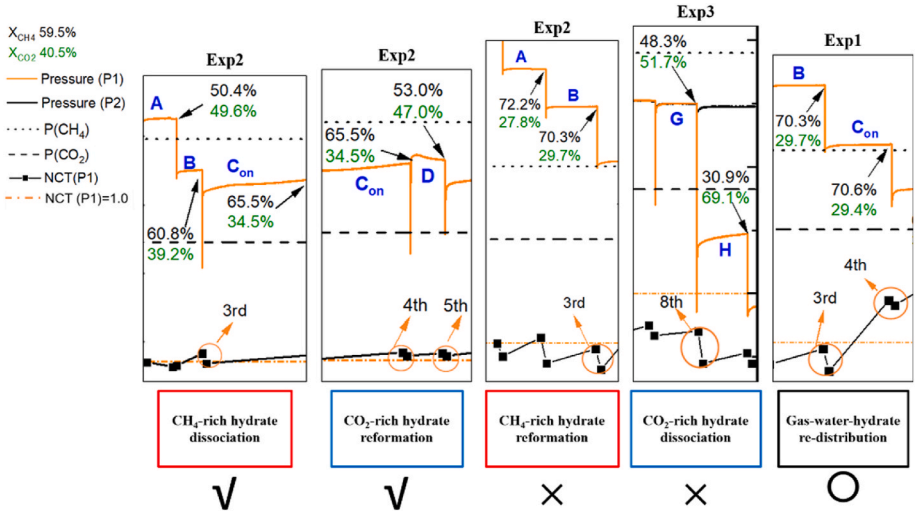

Fig. 21. Five types of characteristics concerning hydrate dissociation, hydrate reformation and gas-water-hydrate redistribution during multistep depressurization. To the benefit of CH_4 recovery and CO_2 storage: √ favorable; × unbeneficial; ○ undetermined.

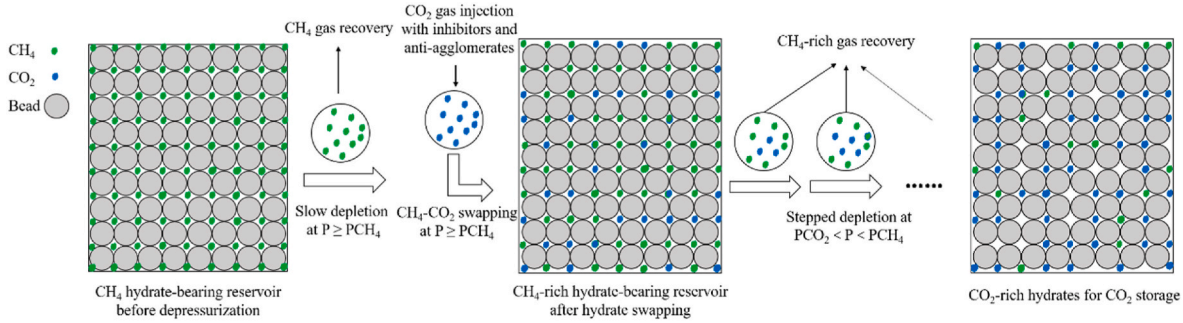

Fig. 22. Schematic of the enhancements of CH_4 recovery and CO_2 storage by multistep depressurization in hydrate-bearing sediment after direct depressurization and hydrate swapping.

undetermined directly. Hence, pore-scale investigation of X-ray CT in this work can be useful to provide supplementary information for varying hydrate mass during MD. To sum up, five types of characteristics of pressure, gas composition and NCT values can be jointly employed to affirm hydrate dissociation, hydrate reformation and gas-water-hydrate redistribution, eventually contributing to scheme design for enhancement of CH_4 production and CO_2 storage.

It was confirmed above that CH_4-rich hydrate dissociation, CO_2-rich hydrate reformation and gas-water-hydrate redistribution promoted CH_4 recovery and CO_2 storage. The schematic of enhancements behind MD after direct depressurization and hydrate swapping is illustrated in Fig. 22. First of all, CH_4 hydrate reservoir is exploited by direct/slow depressurization to produce pure CH_4 gas at depletion pressures above PCH_4. The majority of CH_4 gas produced comes from free gas zone in hydrate-bearing reservoir or partial CH_4 hydrate dissociation due to chemical discrepancy. After that, CO_2 gas together with inhibitors and anti-agglomerates is injected into the depleted CH_4 hydrate reservoir to perform CH_4–CO_2 swapping exploitation at pressures above PCH_4. The purpose of keeping above-PCH_4 pressure is to maintain the mechanical stability of hydrate-bearing sediments without dissociating massive CH_4 hydrates, while CO_2 injection triggered CO_2 hydrate formation acting as the skeleton to increase HBS mechanical stability. The inhibitors and anti-agglomerates are introduced to prevent CO_2 hydrate blockage at the injection point and thus enlarge CO_2 diffusion area. The key point is to conduct well-controlled schemes of multistep depressurization on CH_4-rich hydrates with CH_4-rich gas production and CO_2-rich hydrate storage at depletion pressures between PCO_2 and PCH_4.

4. Conclusions

Morphologies and compositions of CH_4/CO_2 hydrates in hydrate-bearing sediment play vital roles during exploitation. Multistep depressurization (MD) was conducted on hydrate-bearing core by X-ray computed tomography (CT). The distributions of co-existing phases (gas, water and hydrate) and kinetic data (pressures and gas compositions) were combined for improved understandings of hydrate morphology evaluation and fluid migration. The influences of sediment particle sizes and additive L-methionine on CH_4 gas recovery and CO_2 hydrate storage were examined. The major conclusions were summarized as follows.

- Pore-scale hydrate morphologies and distribution showed dispersed pore-filling hydrates, in the shapes of clusters or crusts, formed heterogeneously within pore spaces in core.
- Varying hydrate morphologies and corresponding pressure variations indicated existences of concurrent hydrate dissociation and hydrate reformation in different pores during MD.
- Artificial core with particle size of 3 mm presented more apparent hydrate dissociation and reformation during MD due to its sufficient pore connectivity and mass transfer, which was beneficial to the hydrate exploitation efficiencies.
- L-methionine enhanced CO_2 storage by 20.7% and CH_4 gas fraction by 17.5 mol% by mainly promoting CO_2-rich hydrate formation, proving it is beneficial to CH_4 gas recovery and CO_2 hydrate storage.
- Five-type characteristics of hydrate compositions, hydrate variations and fluid migration were determined during MD to guide efficient CH_4/CO_2 hydrate exploitation.
- Reservoir pressures need to be reduced in steps and controlled between CH_4 hydrate stability pressure and CO_2 hydrate stability pressure for high-efficient exploitation of CH_4/CO_2 hydrates.

From these results, the presented multistep depressurization in this study is recommended for application during CH_4/CO_2 hydrate exploitation. Production schemes should pay more attention to achieving CH_4-rich hydrate dissociation and CO_2-rich hydrate reformation. This will benefit highly-efficient CH_4 gas recovery and CO_2 hydrate storage in the pilot-scale test. Future work is suggested in characterizing and identifying different occurrences and saturations of CH_4/CO_2 hydrates in sediment for targeted and improved depressurization exploitation.

Credit author statement

Qian Ouyang: Writing – original draft, Investigation, Formal analysis, Validation, Visualization, Data curation, Writing – review & editing. Jyoti Shanker Pandey: Conceptualization, Methodology, Supervision, Writing – review & editing, Resources. Yao Xu: Investigation, Formal analysis. Nicolas von Solms: Supervision, Project administration, Funding acquisition.

Declaration of competing interest

The authors declare that they have no known competing financial interests or personal relationships that could have appeared to influence the work reported in this paper.

Data availability

Data will be made available on request.

Acknowledgements

The authors gratefully acknowledge the support received from Department of Chemical and Biochemical Engineering, Technical University of Denmark, and Scholarship of Guangzhou Elite Plan. Dr. Armin Afrough and Hossein Safari are appreciated for providing advice on CT data analysis. Special thanks to Tran Thuong Dang and Duc Thuong Vu for technician assistance on experiment, and Xu Li for image and figure improvement.

Appendix A. Supplementary data

Supplementary data to this article can be found online at https://doi.org/10.1016/j.jgsce.2023.204952.

References

Abu Hassan, M.H., Sher, F., Zarren, G., Suleiman, N., Tahir, A.A., Snape, C.E., 2020. Kinetic and thermodynamic evaluation of effective combined promoters for CO_2 hydrate formation. J. Nat. Gas Sci. Eng. 78, 103313 https://doi.org/10.1016/j.jngse.2020.103313.

Bavoh, C.B., Lal, B., Osei, H., Sabil, K.M., Mukhtar, H., 2019. A review on the role of amino acids in gas hydrate inhibition, CO_2 capture and sequestration, and natural gas storage. J. Nat. Gas Sci. Eng. 64, 52–71. https://doi.org/10.1016/j.jngse.2019.01.020.

Boswell, R., Collett, T.S., 2011. Current perspectives on gas hydrate resources. Energy Environ. Sci. 4, 1206–1215. https://doi.org/10.1039/c0ee00203h.

Cai, Y., Chen, Y., Li, Q., Li, L., Huang, H., Wang, S., Wang, W., 2017. CO_2 hydrate formation promoted by a natural amino acid l-methionine for possible application to CO_2 capture and storage. Energy Technol 5, 1195–1199. https://doi.org/10.1002/ente.201600731.

Cha, M., Shin, K., Lee, H., Moudrakovski, I.L., Ripmeester, J.A., Seo, Y., 2015. Kinetics of methane hydrate replacement with carbon dioxide and nitrogen gas mixture using in situ NMR spectroscopy. Environ. Sci. Technol. 49, 1964–1971. https://doi.org/10.1021/es504888n.

Chen, L., Feng, Y., Kogawa, T., Okajima, J., Komiya, A., Maruyama, S., 2018. Construction and simulation of reservoir scale layered model for production and utilization of methane hydrate: the case of Nankai Trough Japan. Energy 143, 128–140. https://doi.org/10.1016/j.energy.2017.10.108.

Chen, Y., Gao, Y.H., Chen, L.T., Wang, X.R., Liu, K., Sun, B.J., 2019. Experimental investigation of the behavior of methane gas hydrates during depressurization-assisted CO_2 replacement. J. Nat. Gas Sci. Eng. 61, 284–292. https://doi.org/10.1016/j.jngse.2018.11.015.

CSM. Colorado School of Mines Hydrate Software 2015 n.d. http://hydrates.mines.edu/CHR/Software.html.

Dai, S., Santamarina, J.C., Waite, W.F., Kneafsey, T.J., 2012. Hydrate morphology: physical properties of sands with patchy hydrate saturation. J. Geophys. Res. Solid Earth 117.

Davies, S.R., Sloan, E.D., Sum, A.K., Koh, C.A., 2010. In situ studies of the mass transfer mechanism across a methane hydrate film using high-resolution confocal Raman spectroscopy. J. Phys. Chem. C 114, 1173–1180. https://doi.org/10.1021/jp909416y.

Englezos, P., Kalogerakis, N., Dholabhai, P.D., Bishnoi, P.R., 1987. Kinetics of formation of methane and ethane gas hydrates. Chem. Eng. Sci. 42, 2647–2658. https://doi.org/10.1016/0009-2509(87)87015-X.

Farahani, V.M., Guo, X., Zhang, L., Yang, M., Hassanpouryouzband, A., Zhao, J., Yang, J., Song, Y., Tohidi, B., 2021. Effect of thermal formation/dissociation cycles on the kinetics of formation and pore-scale distribution of methane hydrates in porous media: a magnetic resonance imaging study. Sustain. Energy Fuels 5, 1567–1583. https://doi.org/10.1039/d0se01705a.

Gong, L., Nie, L., Xu, Y., 2020. Geometrical and topological analysis of pore space in sandstones based on x-ray computed tomography. Energies 13, 3774.

He, G., Luo, X., Zhang, H., Bi, J., 2018. Pore-scale identification of multi-phase spatial distribution of hydrate bearing sediment. J. Geophys. Eng. 15, 2310–2317. https://doi.org/10.1088/1742-2140/aaba10.

He, J., Li, X., Chen, Z., You, C., Peng, H., Zhang, Z., 2022. Sustainable hydrate production using intermittent depressurization in hydrate-bearing reservoirs connected with water layers. Energy 238, 121752. https://doi.org/10.1016/j.energy.2021.121752.

Heeschen, K.U., Abendroth, S., Priegnitz, M., Spangenberg, E., Thaler, J., Schicks, J.M., 2016. Gas production from methane hydrate: a laboratory simulation of the multistage depressurization test in mallik, northwest territories, Canada. Energy Fuels 30, 6210–6219. https://doi.org/10.1021/acs.energyfuels.6b00297.

Iassonov, P., Gebrenegus, T., Tuller, M., 2009. Segmentation of X-ray computed tomography images of porous materials: a crucial step for characterization and quantitative analysis of pore structures. Water Resour. Res. 45 https://doi.org/10.1029/2009wr008087.

Jin, S., Nagao, J., Takeya, S., Jin, Y., Hayashi, J., Kamata, Y., Ebinuma, T., Narita, H., 2006. Structural investigation of methane hydrate sediments by microfocus X-ray computed tomography technique under high-pressure conditions. Jpn. J. Appl. Phys. 45, L714–L716. https://doi.org/10.1143/jjap.45.l714.

Jin, S., Takeya, S., Hayashi, J., Nagao, J., Kamata, Y., Ebinuma, T., Narita, H., 2004. Structure analyses of artificial methane hydrate sediments by microfocus X-ray computed tomography. Jpn. J. Appl. Phys. 43, 5673–5675. https://doi.org/10.1143/jjap.43.5673.

Kashif, M., Cao, Y., Yuan, G., Asif, M., Javed, K., Mendez, J.N., Khan, D., Miruo, L., 2019. Pore size distribution, their geometry and connectivity in deeply buried Paleogene Es1 sandstone reservoir, Nanpu Sag, East China. Petrol. Sci. 16, 981–1000.

Kneafsey, T.J., Tomutsa, L., Moridis, G.J., Seol, Y., Freifeld, B.M., Taylor, C.E., Gupta, A., 2007. Methane hydrate formation and dissociation in a partially saturated core-scale sand sample. J. Petrol. Sci. Eng. 56, 108–126. https://doi.org/10.1016/j.petrol.2006.02.002.

Kou, X., Feng, J.C., Li, X.S., Wang, Y., Chen, Z.Y., 2022. Memory effect of gas hydrate: influencing factors of hydrate reformation and dissociation behaviors. Appl. Energy 306, 118015. https://doi.org/10.1016/j.apenergy.2021.118015.

Kou, X., Li, X.-S., Wang, Y., Liu, J.-W., Chen, Z.-Y., 2021. Effects of gas occurrence pattern on distribution and morphology characteristics of gas hydrates in porous media. Energy 226, 120401. https://doi.org/10.1016/j.energy.2021.120401.

L'Orange Seigo, S., Dohle, S., Siegrist, M., 2014. Public perception of carbon capture and storage (CCS): a review. Renew. Sustain. Energy Rev. 38, 848–863. https://doi.org/10.1016/j.rser.2014.07.017.

Lei, L., Seol, Y., Jarvis, K., 2018. Pore-scale visualization of methane hydrate-bearing sediments with micro-CT. Geophys. Res. Lett. 45, 5417–5426.

Li, B., Li, X.-S., Li, G., 2014. Kinetic studies of methane hydrate formation in porous media based on experiments in a pilot-scale hydrate simulator and a new model. Chem. Eng. Sci. 105, 220–230. https://doi.org/10.1016/j.ces.2013.11.016.

Li, G., Wu, D.M., Li, X.S., Zhang, Y., Lv, Q.N., Wang, Y., 2017. Experimental investigation into the production behavior of methane hydrate under methanol injection in quartz sand. Energy Fuels 31, 5411–5418. https://doi.org/10.1021/acs.energyfuels.7b00464.

Li, X., Liu, M., Li, Q., Pang, W., Chen, G., Sun, C., 2023. Visual study on methane hydrate formation and depressurization-induced methane hydrate dissociation processes in a micro-packed bed reactor. Fuel 332, 125980. https://doi.org/10.1016/j.fuel.2022.125980.

Li, X.Y., Li, X.S., Wang, Y., Liu, J.W., Hu, H.Q., 2020. The determining factor of hydrate dissociation rate in the sediments with different water saturations. Energy 202, 117690. https://doi.org/10.1016/j.energy.2020.117690.

Liu, X., Ren, J., Chen, D., Yin, Z., 2022. Comparison of SDS and L-Methionine in promoting CO_2 hydrate kinetics: implication for hydrate-based CO_2 storage. Chem. Eng. J. 438, 135504 https://doi.org/10.1016/j.cej.2022.135504.

Lu, H., Kawasaki, T., Ukita, T., Moudrakovski, I., Fujii, T., Noguchi, S., Shimada, T., Nakamizu, M., Ripmeester, J., Ratcliffe, C., 2011. Particle size effect on the saturation of methane hydrate in sediments – constrained from experimental results. Mar. Petrol. Geol. 28, 1801–1805. https://doi.org/10.1016/j.marpetgeo.2010.11.007.

Luo, T., Li, Y., Sun, X., Shen, S., Wu, P., 2018. Effect of sediment particle size on the mechanical properties of CH_4 hydrate-bearing sediments. J. Petrol. Sci. Eng. 171, 302–314. https://doi.org/10.1016/j.petrol.2018.07.054.

Lv, J., Zhao, J., Jiang, L., Liu, Y., Mu, H., 2020. A review of micro computed tomography studies on the gas hydrate pore habits and seepage properties in hydrate bearing sediments. J. Nat. Gas Sci. Eng. 83, 103555 https://doi.org/10.1016/j.jngse.2020.103555.

Max, M.D., 2003. Natural Gas Hydrate in Oceanic and Permafrost Environments. Springer Science & Business Media.

McGlade, C., Speirs, J., Sorrell, S., 2013. Unconventional gas – a review of regional and global resource estimates. Energy 55, 571–584. https://doi.org/10.1016/j.energy.2013.01.048.

Mikami, J.U.N., Masuda, Y., Uchida, T., Satoh, T., Takeda, H., 2006. Dissociation of natural gas hydrates observed by X-ray CT scanner. Ann. N. Y. Acad. Sci. 912, 1011–1020. https://doi.org/10.1111/j.1749-6632.2000.tb06856.x.

Misyura, S.Y., 2016. The influence of porosity and structural parameters on different kinds of gas hydrate dissociation. Sci. Rep. 6, 1–10.

Miyazaki, K., Masui, A., Aoki, K., Sakamoto, Y., Yamaguchi, T., Okubo, S., 2010. Strain-rate dependence of triaxial compressive strength of artificial methane-hydrate-bearing sediment. Int. J. Offshore Polar Eng. 20.

Nguyen, N.N., La, V.T., Huynh, C.D., Nguyen, A.V., 2022. Technical and economic perspectives of hydrate-based carbon dioxide capture. Appl. Energy 307, 118237. https://doi.org/10.1016/j.apenergy.2021.118237.

Ouyang, Q., Pandey, J.S., von Solms, N., 2022a. Critical parameters influencing mixed CH_4/CO_2 hydrates dissociation during multistep depressurization. Fuel 320, 123985. https://doi.org/10.1016/j.fuel.2022.123985.

Ouyang, Q., Pandey, J.S., von Solms, N., 2022b. Insights into multistep depressurization of CH_4/CO_2 mixed hydrates in unconsolidated sediments. Energy 260, 125127. https://doi.org/10.1016/j.energy.2022.125127.

Pan, Z., Liu, Z., Zhang, Z., Shang, L., Ma, S., 2018. Effect of silica sand size and saturation on methane hydrate formation in the presence of SDS. J. Nat. Gas Sci. Eng. 56, 266–280. https://doi.org/10.1016/j.jngse.2018.06.018.

Pandey, G., Poothia, T., Kumar, A., 2022a. Hydrate based carbon capture and sequestration (HBCCS): an innovative approach towards decarbonization. Appl. Energy 326, 119900. https://doi.org/10.1016/j.apenergy.2022.119900.

Pandey, J.S., Daas, Y.J., Karcz, A.P., von Solms, N., 2020a. Enhanced hydrate-based geological CO_2 capture and sequestration as a mitigation strategy to address climate change. Energies 13, 5661. https://doi.org/10.3390/en13215661.

Pandey, J.S., Daas, Y.J., von Solms, N., 2020b. Screening of amino acids and surfactant as hydrate promoter for CO_2 capture from flue gas. Processes 8, 124. https://doi.org/10.3390/pr8010124.

Pandey, J.S., Karantonidis, C., Karcz, A.P., von Solms, N., 2020c. Enhanced CH_4-CO_2 hydrate swapping in the presence of low dosage methanol. Energies 13, 5238. https://doi.org/10.3390/en13205238.

Pandey, J.S., Karantonidis, C., Ouyang, Q., von Solms, N., 2021a. Cyclic depressurization-driven enhanced CH_4 recovery after CH_4–CO_2 hydrate swapping. Energy Fuels 35, 9521–9537. https://doi.org/10.1021/acs.energyfuels.1c00685.

Pandey, J.S., Khan, S., Karcz, A.P., von Solms, N., 2021b. Chemically modified hydrate swapping and hydrate stability during multistage CO_2-N_2 injection schemes. Fuel 299, 120711. https://doi.org/10.1016/j.fuel.2021.120711.

Pandey, J.S., Ouyang, Q., Solms, N.v., 2022b. New insights into the dissociation of mixed CH_4/CO_2 hydrates for CH_4 production and CO_2 storage. Chem. Eng. J. 427, 131915 https://doi.org/10.1016/j.cej.2021.131915.

Pandey, J.S., Solms, N.v., 2019. Hydrate stability and methane recovery from gas hydrate through CH_4–CO_2 replacement in different mass transfer scenarios. Energies 12, 2309. https://doi.org/10.3390/en12122309.

Pandey, J.S., Strand, Ø., von Solms, N., Almenningen, S., Ersland, G., 2022c. Novel pore-scale visualization during CO_2 injection into CH_4 hydrate-saturated porous media. Energy Fuels 36, 10552–10571. https://doi.org/10.1021/acs.energyfuels.1c03878.

Pandey, J.S., Strand, Ø., von Solms, N., Ersland, G., Almenningen, S., 2021c. Direct visualization of CH_4/CO_2 hydrate phase transitions in sandstone pores. Cryst. Growth Des. 21, 2793–2806. https://doi.org/10.1021/acs.cgd.0c01714.

Phillips, S.C., Flemings, P.B., You, K., Meyer, D.W., Dong, T., 2019. Investigation of in situ salinity and methane hydrate dissociation in coarse-grained sediments by slow, stepwise depressurization. Mar. Petrol. Geol. 109, 128–144.

Prasad, P.S.R., Kiran, B.S., 2020. Synergistic effects of amino acids in clathrates hydrates: gas capture and storage applications. Chemical Engineering Journal Advances 3, 100022. https://doi.org/10.1016/j.ceja.2020.100022.

Prasad, P.S.R., Sai Kiran, B., 2018. Clathrate hydrates of greenhouse gases in the presence of natural amino acids: storage, transportation and separation applications. Sci. Rep. 8, 8560. https://doi.org/10.1038/s41598-018-26916-1.

Qureshi, Y., Ali, U., Sher, F., 2021. Part load operation of natural gas fired power plant with CO_2 capture system for selective exhaust gas recirculation. Appl. Therm. Eng. 190, 116808 https://doi.org/10.1016/j.applthermaleng.2021.116808.

Raza, M.A., Hallett, P.D., Liu, X., He, M., Afzal, W., 2019. Surface tension of aqueous solutions of small-chain amino and organic acids. J. Chem. Eng. Data 64, 5049–5056. https://doi.org/10.1021/acs.jced.9b00026.

Sadeq, D., Iglauer, S., Lebedev, M., Rahman, T., Zhang, Y., Barifcani, A., 2018. Experimental pore-scale analysis of carbon dioxide hydrate in sandstone via X-Ray micro-computed tomography. Int. J. Greenh. Gas Control 79, 73–82. https://doi.org/10.1016/j.ijggc.2018.10.006.

Sato, M., Takeya, S., Nagao, J., Jin, S., Kamata, Y., Minagawa, H., Ebinuma, T., Narita, H., 2005. Distribution of hydrate saturation ratios in artificial methane hydrate sediments measured by high-speed X-ray computerized tomography. Jpn. J. Appl. Phys. 44, 473–475. https://doi.org/10.1143/jjap.44.473.

Shi, K., Wei, R., Guo, X., Li, Q., Lv, X., Fan, Q., Dong, H., Yang, L., Zhao, J., Song, Y., 2021. Enhancing gas production from hydrate-bearing reservoirs through depressurization-based approaches: knowledge from laboratory experiments. Energy Fuels 35, 6344–6358. https://doi.org/10.1021/acs.energyfuels.0c04075.

Sloan, E.D., Koh, C.A., 2007. Clathrate Hydrates of Natural Gases. Crc Press.

Song, Y., Xue, K., Zhao, J., Lam, W., Cheng, C., Yang, M., Zhang, Y., Wang, D., Liu, W., Liu, Y., 2013. In situ observation of hydrate growth habit in porous media using magnetic resonance imaging. EPL 101, 36004.

Ta, X.H., Yun, T.S., Muhunthan, B., Kwon, T.H., 2015. Observations of pore-scale growth patterns of carbon dioxide hydrate using X-ray computed microtomography. G-cubed 16, 912–924. https://doi.org/10.1002/2014gc005675.

Tomutsa, L., Freifeld, B., Kneafsey, T.J., Stern, L.A., 2002. X-Ray Computed Tomography Observation of Methane Hydrate Dissociation. OnePetro.

Tupsakhare, S.S., Kattekola, S., Castaldi, M.J., 2017. An application of the results from the large-scale thermal stimulation method of methane hydrate dissociation to the field tests. Ind. Eng. Chem. Res. 56, 4588–4599. https://doi.org/10.1021/acs.iecr.7b00553.

Uchida, T., Ebinuma, T., Takeya, S., Nagao, J., Narita, H., 2002. Effects of pore sizes on dissociation temperatures and pressures of methane, carbon dioxide, and propane hydrates in porous media. J. Phys. Chem. B 106, 820–826.

Uchida, T., Yamazaki, K., Gohara, K., 2016. Gas nanobubbles as nucleation acceleration in the gas-hydrate memory effect. J. Phys. Chem. C 120, 26620–26629.

Waite, W.F., Santamarina, J.C., Cortes, D.D., Dugan, B., Espinoza, D.N., Germaine, J., Jang, J., Jung, J., Kneafsey, T.J., Shin, H., 2009. Physical properties of hydrate-bearing sediments. Rev. Geophys. 47.

Wang, D., Li, Y., Liu, C., Zhan, L., Lu, H., Li, C., Sun, J., Meng, Q., Liu, L., 2020. Study of hydrate occupancy, morphology and microstructure evolution with hydrate dissociation in sediment matrices using X-ray micro-CT. Mar. Petrol. Geol. 113, 104138 https://doi.org/10.1016/j.marpetgeo.2019.104138.

Wang, D., Wang, C., Li, C., Liu, C., Lu, H., Wu, N., Hu, G., Liu, L., Meng, Q., 2018. Effect of gas hydrate formation and decomposition on flow properties of fine-grained quartz sand sediments using X-ray CT based pore network model simulation. Fuel 226, 516–526. https://doi.org/10.1016/j.fuel.2018.04.042.

Wu, N., Li, Y., Chen, Q., Liu, C., Jin, Y., Tan, M., Dong, L., Hu, G., 2021. Sand production management during marine natural gas hydrate exploitation: review and an innovative solution. Energy Fuels 35, 4617–4632. https://doi.org/10.1021/acs.energyfuels.0c03822.

Wu, P., Li, Y., Sun, X., Liu, W., Song, Y., 2020. Pore-scale 3D morphological modeling and physical characterization of hydrate-bearing sediment based on computed tomography. J. Geophys. Res. Solid Earth 125. https://doi.org/10.1029/2020jb020570.

Wu, R., Kozielski, K.A., Hartley, P.G., May, E.F., Boxall, J., Maeda, N., 2013. Probability distributions of gas hydrate formation. AIChE J. 59, 2640–2646.

Yang, J., Dai, X., Xu, Q., Liu, Z., Zan, C., Long, W., Shi, L., 2021. Pore-scale study of multicomponent multiphase heat and mass transfer mechanism during methane hydrate dissociation process. Chem. Eng. J. 423, 130206 https://doi.org/10.1016/j.cej.2021.130206.

Yang, L., Zhao, J., Liu, W., Li, Y., Yang, M., Song, Y., 2015. Microstructure observations of natural gas hydrate occurrence in porous media using microfocus X-ray computed tomography. Energy Fuels 29, 4835–4841. https://doi.org/10.1021/acs.energyfuels.5b00881.

Yang, M., Zheng, J.-n., Gao, Y., Ma, Z., Lv, X., Song, Y., 2019. Dissociation characteristics of methane hydrates in South China Sea sediments by depressurization. Appl. Energy 243, 266–273. https://doi.org/10.1016/j.apenergy.2019.03.160.

Yin, Z., Chong, Z.R., Tan, H.K., Linga, P., 2016. Review of gas hydrate dissociation kinetic models for energy recovery. J. Nat. Gas Sci. Eng. 35, 1362–1387. https://doi.org/10.1016/j.jngse.2016.04.050.

Yin, Z., Moridis, G., Chong, Z.R., Linga, P., 2019. Effectiveness of multi-stage cooling processes in improving the CH4-hydrate saturation uniformity in sandy laboratory samples. Appl. Energy 250, 729–747. https://doi.org/10.1016/j.apenergy.2019.05.077.

Zeman, F., 2007. Energy and material balance of CO_2 capture from ambient air. Environ. Sci. Technol. 41, 7558–7563. https://doi.org/10.1021/es070874m.

Zhao, J., Zhang, L., Chen, X., Zhang, Y., Liu, Y., Song, Y., 2016a. Combined replacement and depressurization methane hydrate recovery method. Energy Explor. Exploit. 34, 129–139. https://doi.org/10.1177/0144598715623676.

Zhao, X., Hu, D., Wen, Z., Tang, X., Deng, J., Wang, R., Yi, L., 2021. Geological structures associated with potential gas-hydrate accumulation in the Mohe permafrost, North East China. J. Petrol. Sci. Eng. 197, 108110 https://doi.org/10.1016/j.petrol.2020.108110.

Zhao, Y., Zhao, J., Shi, D., Feng, Z., Liang, W., Yang, D., 2016b. Micro-CT analysis of structural characteristics of natural gas hydrate in porous media during decomposition. J. Nat. Gas Sci. Eng. 31, 139–148. https://doi.org/10.1016/j.jngse.2016.02.054.